Politecnico di Torino

POLITECNICO DI TORINO

Master's Degree in Energy and Nuclear Engineering

Master's Degree Thesis

Characterization of innovative materials for fusion applications

Supervisor

Prof. Monica FERRARIS

Candidate

Francesca BUSSI

December 2024

Acknowledgements

Desidero iniziare ringraziando la Professoressa Monica Ferraris per avermi guidato in questo percorso. Sarò sempre grata per il Suo costante supporto in questi mesi e per le opportunità di crescita che mi ha offerto.
Un sentito ringraziamento va anche al Dr. Dario Alidoost, che mi ha seguito con pazienza lungo il lavoro di tesi, aiutandomi a superare le difficoltà e offrendo sempre i consigli giusti al momento giusto.

A mamma, papà e Matteo. Non penso riuscirò mai a dimostrare la mia gratitudine per il continuo sostegno che mi avete dato in questi anni. Avete sempre creduto nelle mie capacità, soprattutto nei momenti in cui ero la prima a non farlo. E non importa dove andrò, casa sarà sempre un luogo nelle colline dove c'è un gatto che corre.

A Nina e Zio. Siete sempre stati presenti nella mia vita, e se sono diventata la persona che sono oggi è anche grazie a voi.

A Matilde. Per fortuna avevo quel portapenne la prima settimana di università, altrimenti chissà dove sarei adesso. Non penso sarei mai sopravvissuta a questi anni senza la tua amicizia e il tuo continuo supporto. Mi hai sempre spinto ad essere la migliore versione di me stessa. Credo, e spero, sarà così per tanto tempo.

Ai miei amichetti di Torino, che non nomino uno per uno solo perché altrimenti

questi ringraziamenti diventano più lunghi della tesi. Grazie a voi ho trovato un gruppo di amici con cui condividere i momenti di più grande gioia come oggi, ma anche con cui affrontare tutte le difficoltà. Non importa dove la vita ci porterà, so che ci saremo sempre l'uno per l'altro. E se ricorderò questi anni come un periodo sereno della mia vita è soprattutto grazie a voi.

A Federica. Sarò sempre riconoscente per la chiusura della scuola elementare di Cervignasco. Perché, come ci piace ripetere, noi due abbiamo solo fatto l'ultimo anno di elementari insieme, ma nonostante tutto, siamo ancora qua, a sostenerci anno dopo anno.

A Ilaria e Jenny. Siete le costanti della mia vita da più di un decennio. Siete stata la parte migliore della mia adolescenza e so che sarete altrettanto indispensabili nella mia vita adulta. Anche se la vita ci ha portato in luoghi lontani, sono certa che ci ritroveremo sempre.

A Noemi. Ringrazio Berlino per averci fatto incontrare. Anche se quel periodo è stato solo una parentesi della mia vita, sono contenta che tu sia rimasta anche nella vita reale. Mi mancheranno sempre un po' le nostre tisane notturne su quel divano al quinto piano.

A tutte le persone che ho conosciuto e che mi hanno reso chi sono oggi. Come dice la frase sulla prima pagina del mio diario, sono un mosaico di tutte le persone che ho amato nella mia vita, anche solo per un attimo. E guardando le persone da cui sono circondata oggi, anche da coloro che non sono qui fisicamente, penso di

potermi ritenere fiera della persona che sono diventata.

Abstract

Nuclear fusion represents one of the most ambitious promises for clean and sustainable energy production, with projects like ITER and DEMO aimed at demonstrating the feasibility of large-scale fusion reactors. Within the European context, EUROfusion plays a crucial role in coordinating and supporting research on advanced materials necessary to withstand the extreme conditions inside fusion reactors. This thesis is part of the EUROfusion project and focuses specifically on the characterization of CuCrZr alloy, a key material whose thermal and mechanical properties make it well-suited for structural components, such as heat sink materials in high heat flux components.

The mechanical and thermo-mechanical characterization of CuCrZr is crucial to ensure its resilience under the high temperatures and stresses typical of a fusion environment. This analysis includes determining key properties such as Young's modulus, shear modulus, Poisson's ratio, and the coefficient of thermal expansion These parameters provide insight into the material's capacity to retain structural integrity, supporting predictions of its behavior under operational conditions and contributing to the design and safety of future fusion reactors. Additionally, advanced tensile testing—including precise measurements of diameter in the necking region and calculations of the radius of curvature during deformation—offers a deeper understanding of CuCrZr's performance under stress.

Table of Contents

List of Tables

List of Figures

Chapter 1

Introduction

As the issue of climate change becomes more pressing in today's society, finding new pathways to reduce carbon emissions is crucial. The increase in the total energy demand through 2050 [1] is coupled with the European goal of climate neutrality by 2050 [2]. Because of this coupling, even though coal, oil and gas are a key element to sustain the world's economic development [3], their use must decrease due to the environmental challenges they create. The best solution is to substitute the aforementioned fossil fuels with clean energy sources [4].

In this context, nuclear fusion is emerging as a promising option for electricity generation, although its feasibility has yet to be fully demonstrated [5]. Fusion energy is often described as the *energy source of the universe*, as the light of the stars is generated by fusion reactions [6]. On the surface of the Sun, weak interactions are sufficient for fusion to occur, thanks to its immense mass. However, in a fusion reactor on Earth, where the available volume is only a fraction of that of a star, the interactions must be significantly stronger to achieve the required reaction rates. The most promising fusion reaction is the deuterium (D) - tritium (T), both hydrogen isotopes [6].

$$D + T = {}^{4}H + n + 17.6\ MeV \tag{1.1}$$

Evaluating this technology requires a focus on two important elements.
TThe first is the availability of fuel, as the deuterium-tritium (D-T) reaction 1.1 is the most likely to be implemented in a fusion reactor. Deuterium (D) is naturally found in hydrogen and it can be obtained through the electrolysis of heavy water [7]. Tritium (T), as of right now, can only be extracted by heavy-water fission reactors. The amount produced per year is enough for the operation of ITER (1.1), but not enough for a commercial electricity-producing fusion plant, as 70 kg of tritium is required per gigawatt of thermal power. Currently, tritium is produced at a rate of 20 kg per year. [8]. The solution lies in the fusion reaction itself: tritium can be bred in the blanket of the reactor thanks to the reaction between the fusion neutrons and the isotope 6-lithium [7]:

$$^6Li + n = {}^4He + T + 4.8\ MeV \tag{1.2}$$

The problem that emerges is the limited availability of lithium in rare earths for which equity issues may arise [6].

Secondly, the fusion reaction (1.1) happens when the two nuclei of deuterium and tritium collide. In order to achieve the collision, the thermalized mixture of deuterium and tritium is confined at energies of 10 keV (about 100 million °C, as $1\ eV \mathrel{\hat{=}} 1.16 \cdot 10^4\ °C$) [6]. At these temperatures, the hydrogen isotopes form a plasma of charged ions and electrons. The plasma is confined by strong magnetic fields in a torus geometry [6]. To realize this confinement, two different configurations have been studied: the *Tokamak* [9] and the *Stellarator* [10]. In both cases, the interaction of the hot plasma with surrounding structures must be addressed. That is why the development of suitable structural materials is crucial for the advancement of fusion energy feasibility, as the components of the reactor are subjected to intense mechanical, heat and electromagnetic loads [11]. It is also important to consider that the materials operate in a neutron-interactive environment. Therefore, low activation characteristics are a critical requirement [12].

It is therefore clear that thorough research is necessary to demonstrate the feasibility of the technology. This is precisely the goal of ITER (par. 1.1).

1.1 ITER

ITER's main goal is to verify the scientific and technological achievability of fusion energy [13]. It is expected to be the first magnetic confinement device to produce a net surplus of fusion energy: with an input of 50 MW and a fusion gain of $Q = 10$ in the plasma, the expected thermal output is 500 MW [14]. As an experimental plant, ITER is not designed to generate electricity by the exploitation of the heat produced by the plasma [15]. However, it is of great significance as "the realisation of fusion energy depends completely on ITER's success" [14]. ITER employs a *tokamak* configuration for the magnetic confinement of the plasma. The cross-section of the entire structure of the tokamak is shown in Figure 1.1.

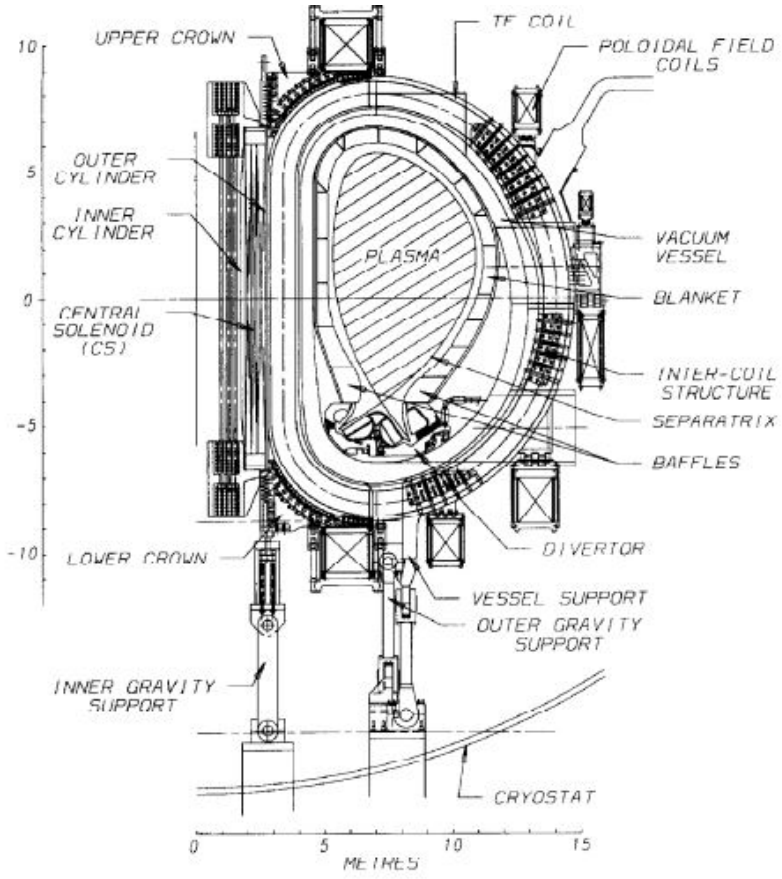

Figure 1.1: ITER's tokamak cross section [15]

The components that interact directly with the plasma are the *blanket* and the *divertor*. These are the most demanding parts of the project due to the high level of neutron irradiation and intense heat flux [16].
The blanket is the primary interface with the plasma and must meet several specific requirements. Its main function is to protect the vacuum vessel and the field coils from thermal and neutronic loads [17].

The divertor's role is to ensure the purity of the plasma and the extraction of power [15, 18] and it is located at the bottom of the vacuum vessel [14, 17].
The research on the material for the aforementioned components has been focused on the use of industrially available materials [16], with specific modifications in order to meet the demands of their applications. For example, CuCrZr, whose characteristics make it the best candidate for the heat sink in the divertor (ch. 1.3.1), has undergone stringent specification changes regarding the concentration of Cr and Zr in order to enhance its strength properties [16].

Another important aspect of the ITER project is the *Test Blanket Module* program, (TBM) [19], which will be developed in later stages [14]. The program aims to gather meaningful data for the performance of the breeding blanket. The breeding blanket is essential for the production of tritium and heat extraction for electricity generation [19]. This program is of critical importance, as these characteristics are required for every subsequent step to make fusion energy feasible [20], starting from DEMO (par. 1.2).

1.2 DEMO

DEMO, the Fusion Demonstration Power Plant, is the last step before the commercialisation of fusion energy. It must demonstrate the feasibility of electricity production in a fusion power plant [21].

The main goals of DEMO are as follows: first, tritium self-sufficiency. The

DEMO power plant must incorporate an efficient breeding module in order to enable a fuel closed-loop cycle [21, 22]. Second, generation of power: DEMO's design includes a power generator connected to the grid [22], with an expected net electricity generated of 0.5–0.7 GW [23]. Finally, DEMO must ensure safety and guarantee a low environmental impact [21].

The project is still in its initial stages. Since 2020, the concept stage has been underway, during which the physics and the baseline concept are being refined. The next technical phase is expected to start in the 2030s, which will involve the engineering design. DEMO's construction is planned to start in the 2040s, with the goal of initial operation in the 2050s [24]. This timeline is achievable only if ITER (par. 1.1) is able to achieve its objectives [14].

As it was already said for ITER, an important challenge for DEMO is the research on the structural materials. These materials are subjected to high heat flux and a neutron-interactive environment [25]. The main issues concern the in-vessel components that directly interact with the plasma, specifically the first wall and the divertor [26]. For the former, coated Eurofer is being considered [27], while CuCrZr (par. 1.3.1), previously mentioned, is being considered for the heat sink in the divertor.

1.3 EUROfusion

The projects mentioned in the previous paragraphs (ITER, par. 1.1, DEMO, par. 1.2) are coordinated within Europe by EUROfusion, whose primary objective is to lay the groundwork for fusion power reactors [28]. EUROfusion aims to fulfill its mission by adhering to a structured roadmap (Fig. 1.2) that outlines the pathway toward commercializing energy generated by fusion power plants.

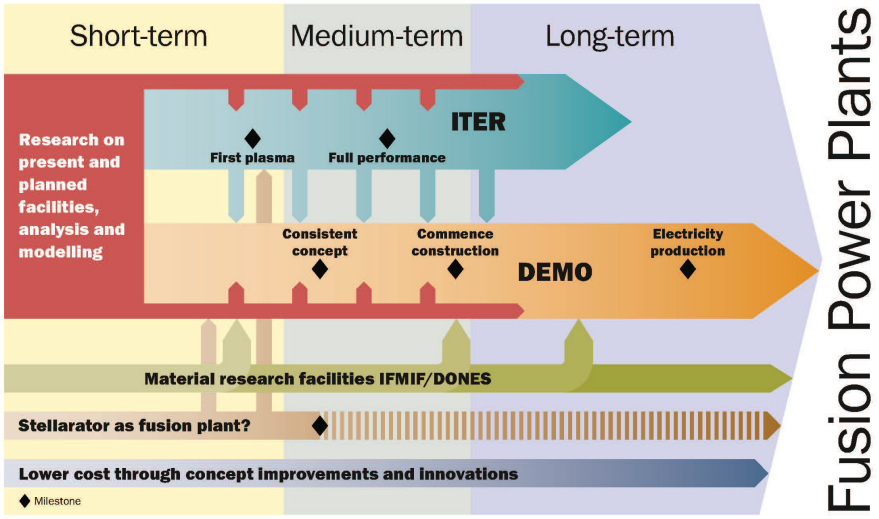

Figure 1.2: EUROfusion roadmap phases [14]

This roadmap is continuously updated to reflect scientific advancements, technological progress, and emerging opportunities [14]. EUROfusion funds research programs across the 26 EU member states that participate in the organization.
A significant portion is dedicated to developing and characterize advanced structural and high heat flux materials for fusion reactor applications, following the EUROfusion Workpackage Materials (WPM). This includes heat sink materials, such as copper alloys, and tungsten-based plasma-facing materials [29]. This thesis specifically focuses on characterizing CuCrZr (par. 1.3.1), the heat sink material for the divertor.

1.3.1 CuCrZr

The choice of material for the high heat flux components of ITER, and subsequently of DEMO, is a major challenge. The amount of heat generated by the plasma that has to be removed by the divertor is an important aspect that generates strict constraints regarding the design of the materials [30]. As said in the previous paragraphs, CuCrZr is the prime candidate as the heat sink material for the divertor.

Pure copper has very good thermal and electrical conductivity. However, its strength is particularly low. For this reason, its application as heat sink is restricted. There are mechanisms that allow to increase the strength of Cu, without compromising the good thermal and electrical conductivity. An example is precipitation hardening, and it's how CuCrZr is formed [31]. This copper alloy is characterized by high thermal and electrical conductivity [32] coupled with higher-temperature strength in comparison to pure copper.

The CuCrZr analysed in this thesis is the so-called ITER-Grade CuCrZr (IG-CuCrZr). This copper alloy is subjected to more stringent contraints regarding its composition and heat treatments [30]. The weight percentages are specified in Table 1.1.

Table 1.1: Composition of CuCrZr-IG

[31]

Chromium (Cr)	$0.6 \sim 0.9$ wt%
Zirconium (Zr)	$0.07 \sim 0.15$ wt%

There are other minor alloying elements, but they are not often mentioned in literature.
In the following chapters, the mechanical (ch. 2) and thermo-physical analysis (par. 3) of CuCrZr to assess the mechanical and thermo-mechanical properties of this copper alloy are performed. Furthermore, the necking (ch. 4) and the variation of the radius of curvature (ch. 5) during tensile testing have been evaluated in detail.

Chapter 2

Mechanical analysis

The mechanical analysis is conducted to calculate the Young modulus, E, the shear modulus, G, and the Poisson ratio, μ. The methods and set-up used for these evaluations are explained in greater detail in the paragraphs *Elastic modulus* (par. 2.1) and *Shear modulus and Poisson ratio* (par. 2.2).

The machine used for the tests is the *IMCE - RFDA HT1600*, which exploits non-destructive methods to asses the aforementioned mechanical properties.

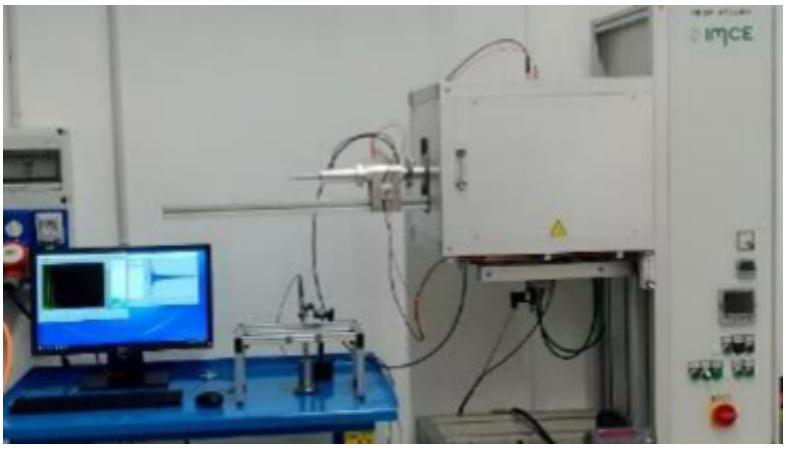

Figure 2.1: Machine used for the evaluation of E, G, μ

It is essential to evaluate the mechanical properties at temperatures ranging from RT (room temperature, 25°C) to 600°C in controlled atmosphere (Argon, Ar).

This condition is imposed in order to minimize the oxidation on the specimen. The chosen geometry of the test specimen is a rectangular beam.

2.1 Elastic modulus

The elastic modulus, also known as Young modulus, E, is an intrinsic material property that measures the material's resistance to deform in the elastic field. It is defined as the slope of the stress-strain (σ-ϵ) curve. The determination of its value can be accomplished through static and dynamic methods. The former method consists of tensile tests and flexural tests. The primary challenges associated with these types of tests are the need for high accuracy in the measurement of the strain and and the increased difficulty of performing measurements at elevated temperatures [33].
For the purposes of this thesis, dynamic methods were implemented, as they are non-destructive and can provide higher accuracy measurements at elevated temperatures. Furthermore, with specific set-ups and specimen geometries, it is possible to measure the shear modulus and Poisson's ratio (par. 2.2) can be calculated.

The dynamic non-destructive method employed is the *resonance and impact excitation* method. The measurement were conducted according to the *E1876–01* standard [34].
To evaluate the elastic modulus, the characteristic vibration frequencies, and in this particular case, the *fundamental flexural resonant frequency* is determined by striking the specimen lightly at the centre of the specimen. It means at the antinode, where there is maximum vibration. This point is highlighted in Figure 2.2 as X1. The beam is supported at the nodes, which are located at 0.224 of the length of the beam [33]. There, the minimum vibrations occur; this particular position is chosen to avoid damping the vibrations.

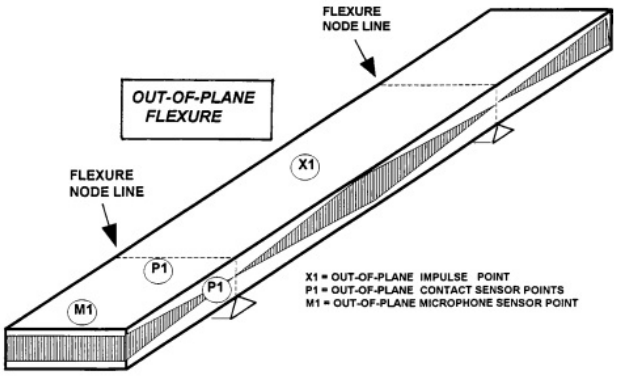

Figure 2.2: Rectangular Specimens Tested for Out-of-Plane Flexure [34]

The frequencies are captured by a microphone with a frequency range sufficient to measure the expected vibrations. The non-contact transducer is positioned at an antinode, ensuring it is close enough to detect the signal without interfering with the specimen. In Figure 2.2, this position is marked as M1. The flexural frequency is then related to the elastic modulus by the following equation:

$$E = 0.9465 \frac{m f_f^2}{b} \frac{L^3}{t^3} T_1 \tag{2.1}$$

Here,

- m is the mass of the beam,
- f_f is the fundamental resonant flexural frequency read by the microphone,
- b is the width of the beam,
- L is the length of the beam,
- t is the thickness of the beam,

- T_1 is a correction factor calculated through the equation

$$T_1 = 1 + 6.585(1 + 0.00752\mu + 0.8109\mu^2)\left(\frac{t}{L}\right)^2 - 0.868\left(\frac{t}{L}\right)^4 - \left[\frac{8.340(1 + 0.2023\mu + 2.173\mu^2)(\frac{t}{L})^4}{1.000 + 6.338(1 + 0.1408\mu + 1.536\mu^2)(\frac{t}{L})^2}\right] \quad (2.2)$$

The geometry parameters of the specimen, meaning the mass, width, length and thickness, are essential. As a matter of fact, during the configuration of the machine, it is required to input them. The software configuration is shown in Figure 2.3.

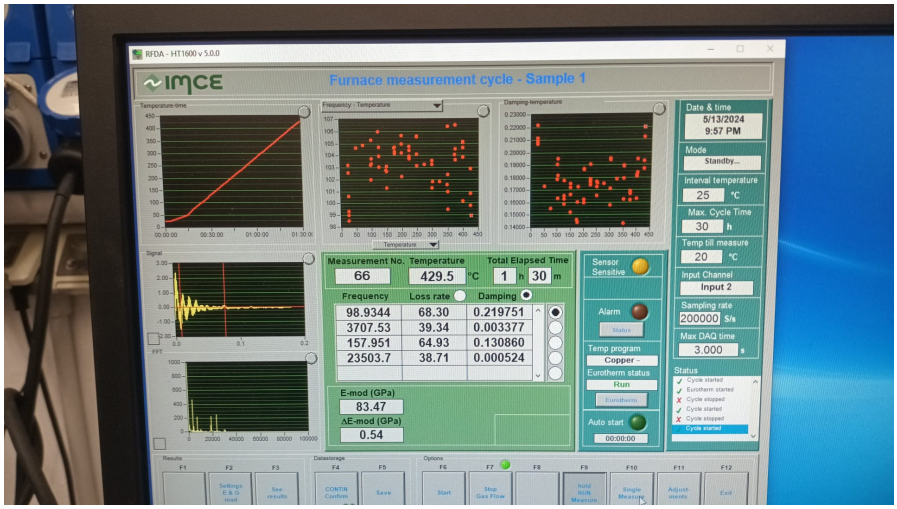

Figure 2.3: Software used for the evaluation of the Young modulus

The frequencies read by the machine depends on the dimensions of the specimen. However, the elastic modulus evaluated remains constant for the same material. When calculating the elastic modulus, the Poisson's ratio is needed to determine the correction factor T_1 (eq. 2.2). By convention and this value is set at 0.275 [33].

2.1.1 Results

As the start of the work on the evaluation of the elastic modulus for CuCrZr, it was important to verify the repeatability of the tests. For this reason, a different test specimen of CuCrZr was used. The first measurements were run on a CuCrZr specimen with the dimensions detailed in Table 2.1.

Table 2.1: Initial dimension of the specimen for elastic modulus measurement

Length	68.96	mm
Width	11	mm
Thickness	4.85	mm
Mass	33.22	g

As was said in the introduction of the mechanical analysis of this section (par. 2), the test was conducted from RT to 600 °C. As only the elastic modulus is being calculated, the set-up used for the measurement is the one decribed in paragraph 2.1 (Fig. 2.2).

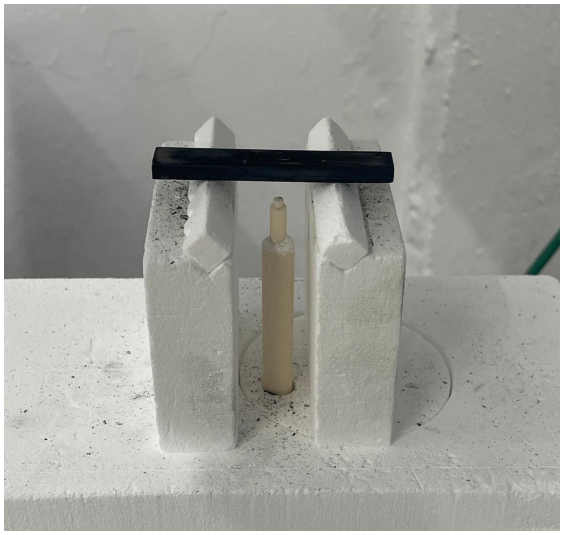

Figure 2.4: Test specimen after the first measurement of elastic modulus in air

At first, the evaluation was conducted in air rather than in a controlled atmosphere, leading to significant oxidation of the specimen, as it can be seen from

Figure 2.4). For the subsequent measurements, the oxidised layer on the test specimen was removed. As a result, the initial dimensions of the beam, shown in table 2.1, changed for each following measurement.

The procedure was repeated three times in air, and the results of the measurements are shown in Figure 2.5.

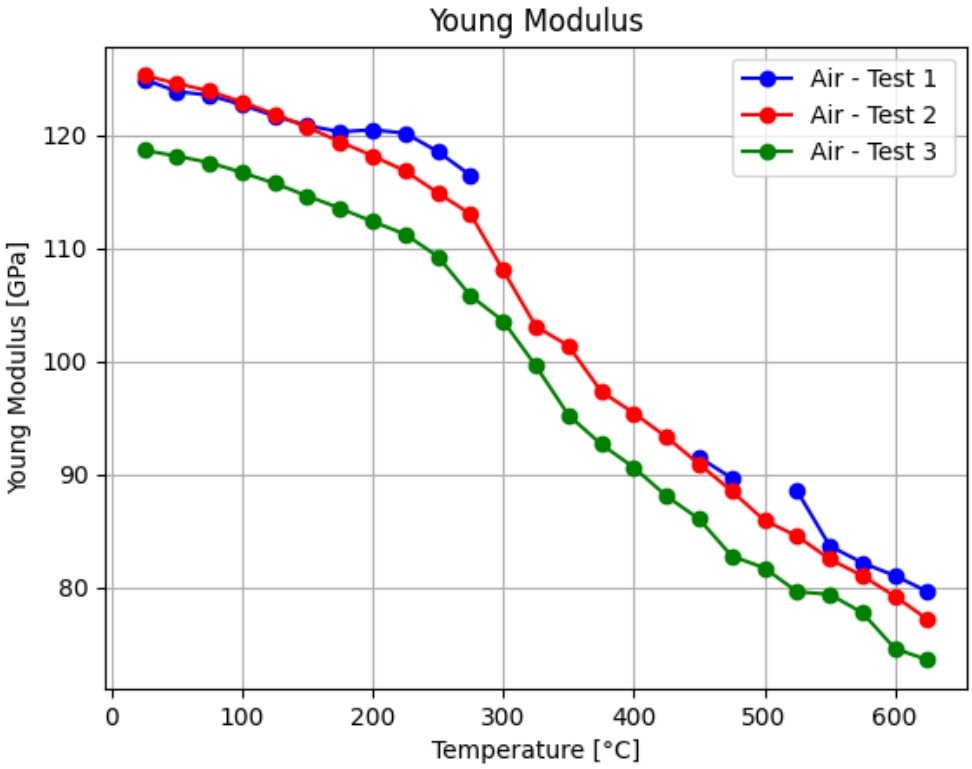

Figure 2.5: Elastic modulus in air

It is of crucial to address the various problems that arose during these initial tests.

The first aspect to notice is that during the first run, indicated in blue in Figure 2.5, from 300°C to 425°C the machine was unable to pick up the correct frequencies to calculate the value of the elastic modulus, resulting in values that were inconsistent with previous measurements. Consequently, these values were discarded. Figure

2.6 illustrates the differences in recorded frequencies.

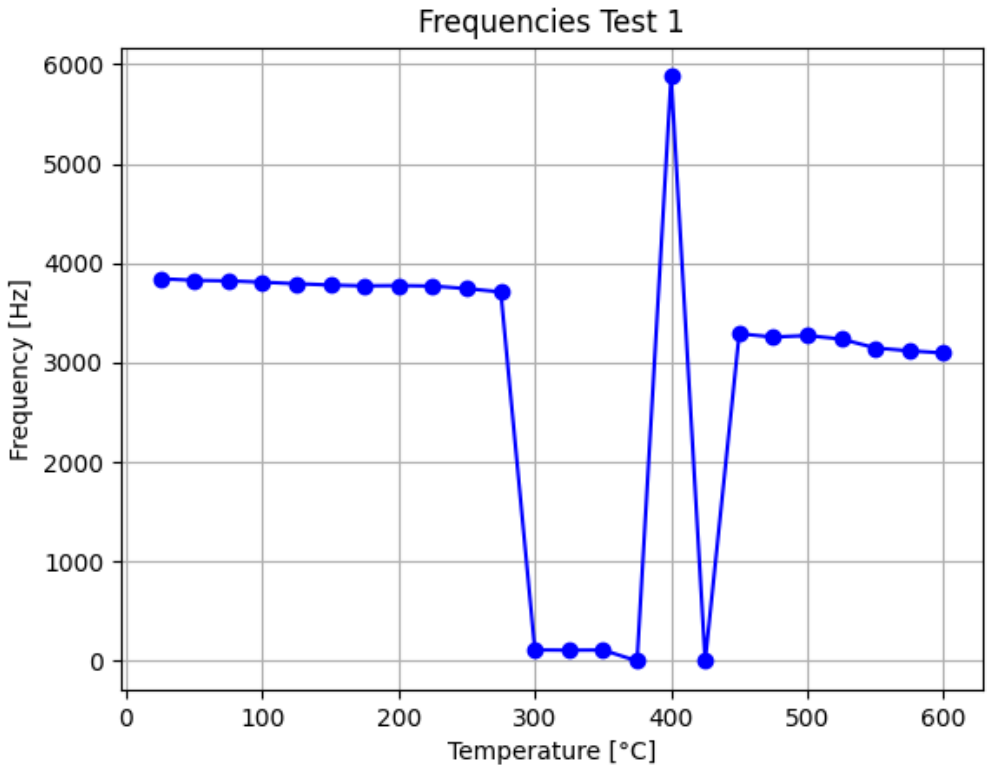

Figure 2.6: Frequency picked up during the first test

From RT to 275°C, the decrease in frequency is congruent with the decrease of the Young modulus, seen in Figure 2.5. This is consistent with the way E is calculated (eq. 2.1). However, starting from 300°C, the microphone began to struggle with accurately recording the frequencies. From 300°C to 375°C, the recorded frequencies are close to 0 Hz, while a peak at 700 Hz is observed at a temperature of 400°C.

To address this issue, a frequency filter was applied, limiting the range to 1000 Hz to 5000 Hz. This adjustment allowed the machine to record a consistent decrement in frequency, which consequently reflected in the elastic modulus values.

During the second measurement (red line in Figure 2.5), at 300°C, the same error encountered in the previous paragraph occurred. However, with the solution already convalidated, it was possible to get all the values required.

Unfortunately the third and last measurement done in air yielded disappointing results. The variation in the elastic modulus values at the same temperature for different measurements was significant, around 3-4 GPa. However, upon further analysis, some inaccuracies in the dimensions entered in the software for the calculation were identified. As mentioned in the introduction, the dimensions of the test specimen directly influence the frequency recorded by the transducer [33], and consequently the value of the Young modulus, that should remain constant at a specific temperature for the same material.

However, the behaviour of the elastic properties of the Cu alloy as the temperature increases is consistent with the existing literature. According to the ITER material handbook [35], the behavior of the elastic modulus as a function of increasing temperature can be described by the following equation:

$$E = 129.2039 - 3.4523 \cdot 10^{-2}\ T - 4.1233 \cdot 10^{-5}\ T^2 \tag{2.3}$$

Figure 2.7 illustrates the behavior across the temperature range of the tests conducted.

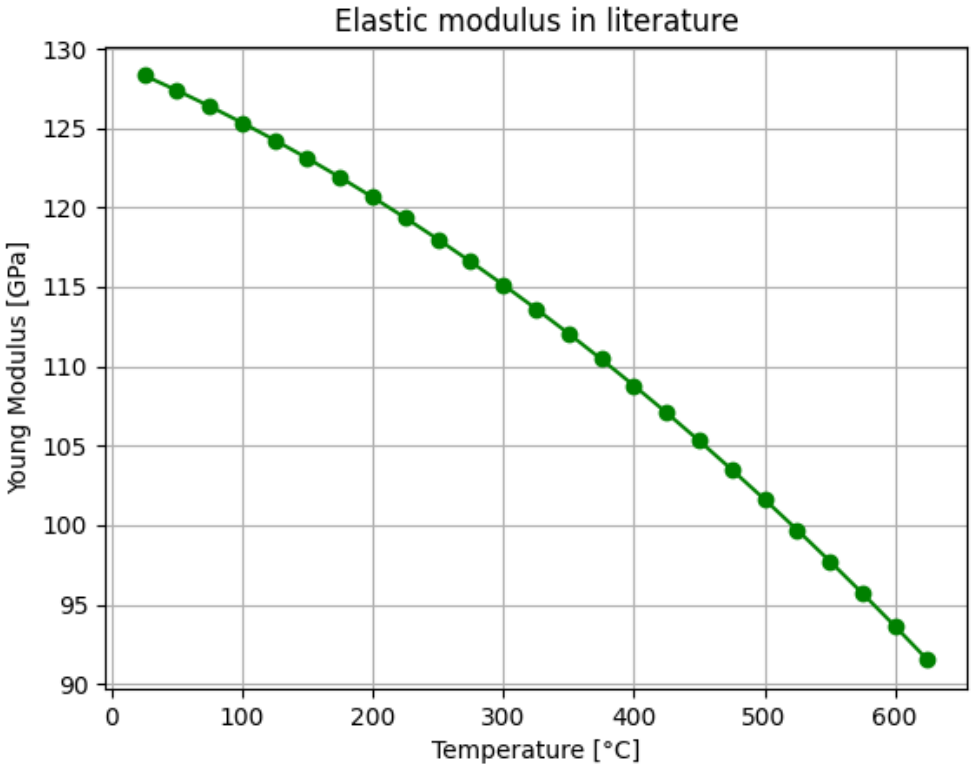

Figure 2.7: Behaviour of elastic modulus in literature [35]

With an increase of temperature, the copper alloy undergoes a thermal expansion (par. 3) which results in a decrease in the stiffness of the specimen. This reduction in stiffness leads to a corresponding decrease in the material's resistance to elastic deformation. Consequently, the elastic modulus, which defines the material's ability to resist deformation in the elastic region, becomes lower. Therefore, the behavior observed in the initial tests is consistent with the expected outcome.

The next tests were run in a controlled atmosphere, from RT to 600°C. The beam used is the same as the one in the previous measurement, with the same set-up shown in Figure 2.2.

The values obtained from these tests are shown in figure 2.8.

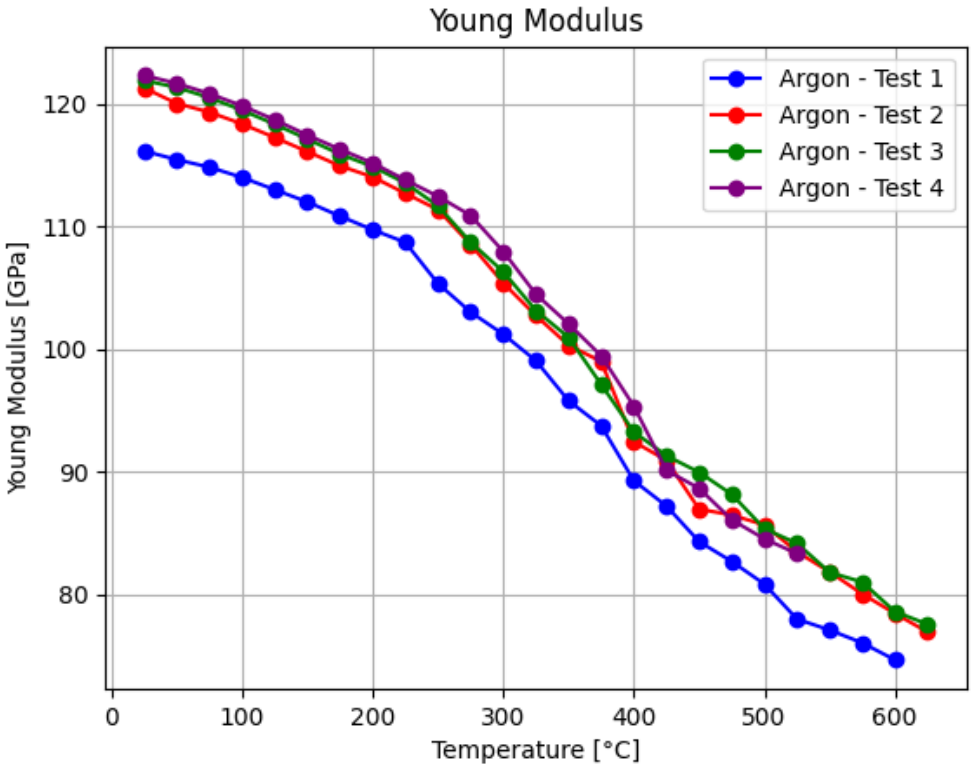

Figure 2.8: Elastic modulus in controlled atmosphere (Ar)

It is clear that an error occurred during the first test. Upon further inspection, the mistake was traced back to the initial input (Fig. 2.3). The dimensions of the specimen entered were those from the third measurement in air (green line in Figure 2.5), without accounting for the removal of the oxidized layer. As a result, the subsequent three tests were conducted with heightened attention to the evaluation of the geometric characteristics of the beam.

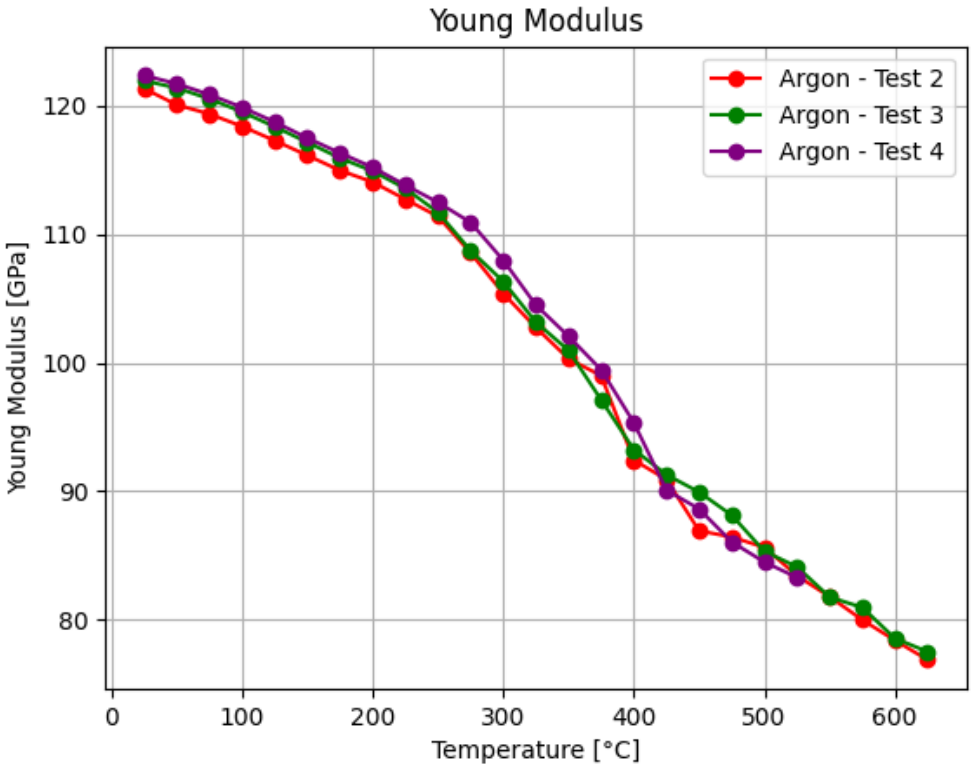

Figure 2.9: Elastic modulus in controlled atmosphere (Ar)

From these last three evaluations, the repeatability of the tests was successfully demonstrated.

By calculating the average of the values obtained from the last three measurements, it was possible to determine the standard deviation of each value in relation to the mean (Fig. 2.10).

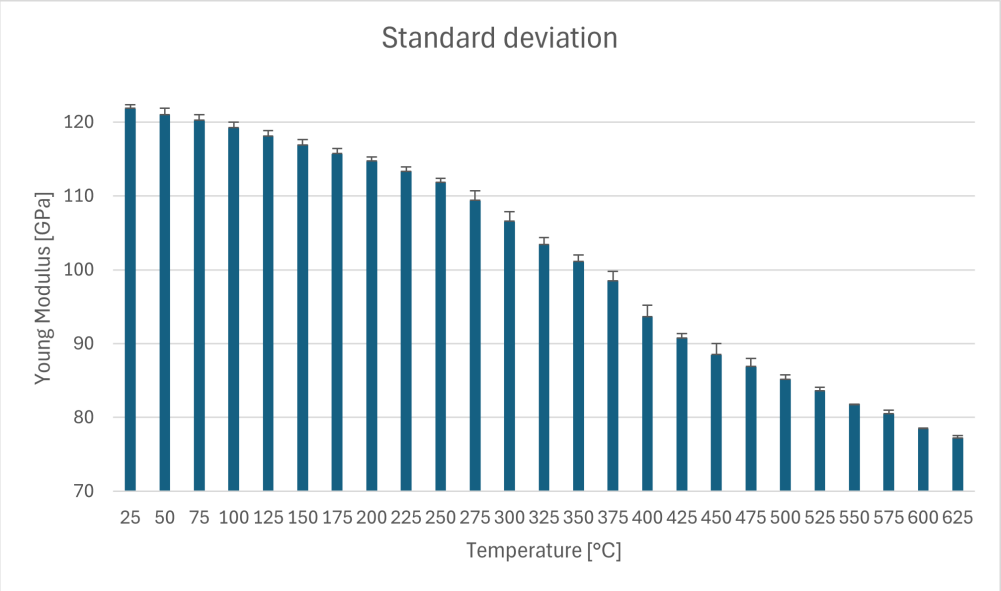

Figure 2.10: Standard deviation of the elastic modulus evaluated in Ar, first specimen

These initial measurements were crucial for assessing errors and identifying the appropriate solutions. Consequently, with the correct CuCrZr specimen, the test could proceed smoothly.

The following evaluations of the elastic modulus were conducted using the correct CuCrZr specimen. As the one used before, it is IG-CuCrZr. The dimensions of the beam are displayed in table 2.2.

Table 2.2: Dimension of the second specimen for elastic modulus measurement

Length	70.13	mm
Width	12.36	mm
Thickness	5.96	mm
Mass	46.30	g

The specimen is subjected to the evaluation of the elastic modulus from RT to 600°C in controlled atmosphere. The values obtained by the two tests are displayed in figure 2.11.

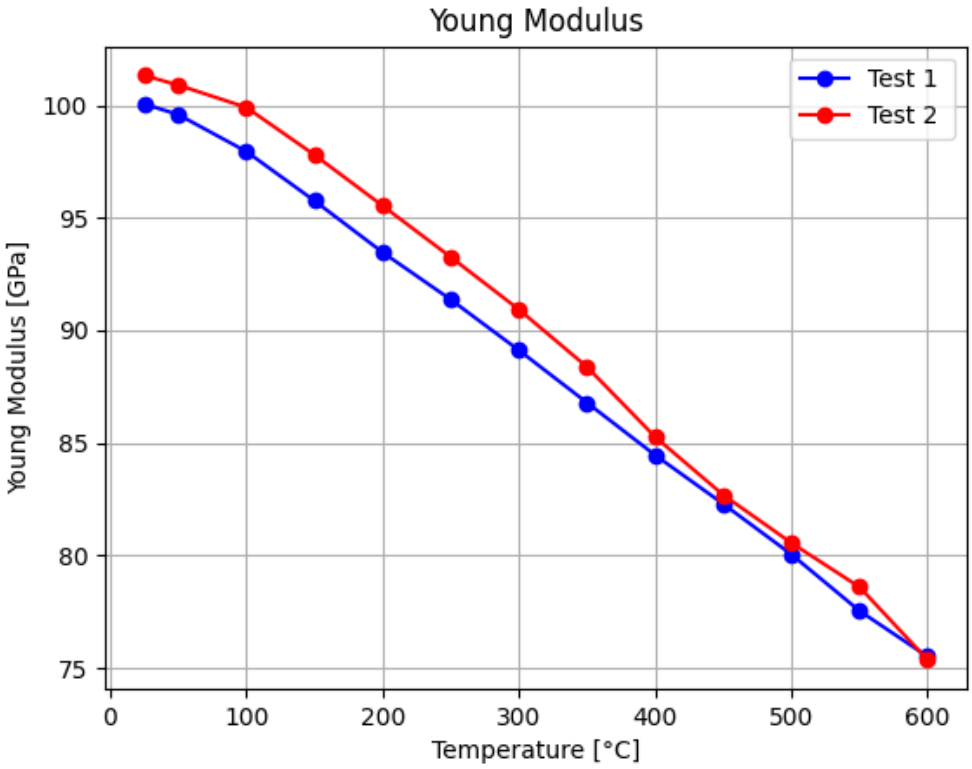

Figure 2.11: Elastic modulus in controlled atmosphere (Ar) with CuCrZr specimen

Even if the tests were run in controlled atmporphere, the specimen was subjected to a small oxidation, as it can be seen in figure 2.12, but in a much lesser extent compared to the previous measurements (Fig. 2.4).

Figure 2.12: Test specimen after first test in Argon

The standard deviation of the values obtained by these two measurements are shown below in figure 2.13

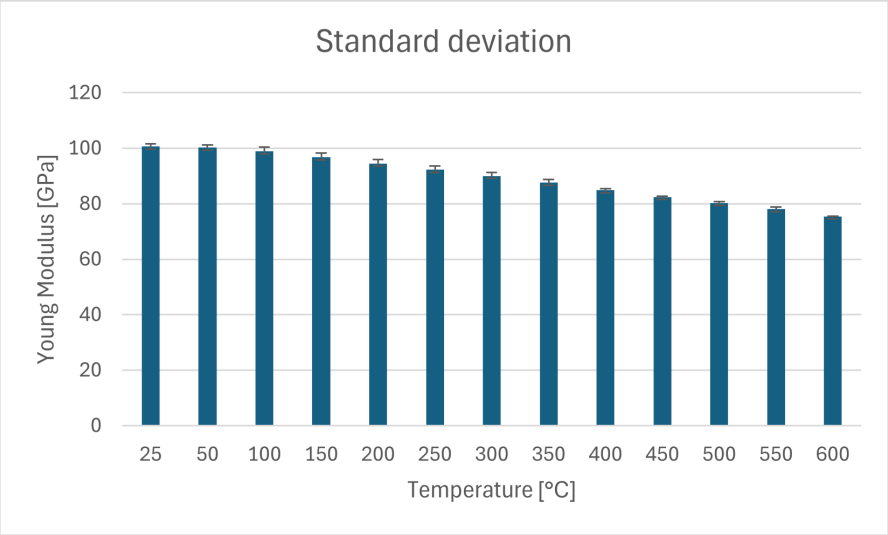

Figure 2.13: Standard deviation of the elastic modulus evaluated in Ar, second specimen

The standard deviaton varies from 0.11 at 600°C to 1.46 at 200°C. These values can be considered acceptable, as the measured elastic modulus is in the order of hundreds GPa.

What is important to notice is that compared to the tests ran on the first specimen (Fig. 2.9) in the same conditions (controlled atmosphere, from RT to 600°C) the values of the Young modulus differ significanty, with discrepancies of up to 20 GPa at the same temperature. The difference in behavior between the first and second specimen can be attributed to the heat treatment experienced by the former. The first specimen was tested several times up to temperature of 650°C which may have altered the microstructure of the alloy due the continuous heating. Such heating can promote precipitation hardening, especially the growth of chromium (Cr) and zirconium (Zr), which can influence the mechanical properties, including the elastic modulus [36]. In contrast, the second specimen of CuCrZr was heated only for the

evaluation of the elastic modulus during the first test (blue line in Figure 2.11). Consequently, the effects of the heating process are not yet apparent.

The next evaluations of the elastic modulus were coupled with the measurement of the shear modulus, G, and the Poisson ratio, μ. The set-up used for these tests and the results are described in paragraph 2.2.

2.2 Shear modulus and Poisson ratio

The shear modulus G, and the Poisson ratio, μ are two mechanical properties intrinsical for each material in the elastic field. The shear modulus describes how a material responds to shear deformation, indicating its stiffness against shearing forces. Conversely, the Poisson ratio is defined as the ratio of the absolute value of the transverse strain to the axial strain when the material is subjected to unidirectional tension or compression. In simple terms, it measures how a material deforms perpendicular to a stress applied in tension or compression along the axial direction.

To evaluate the shear modulus, G, and the Poisson ratio, μ, beside the flexural frequency f_f, as was said in the section *Elastic modulus* (par. 2.1), the machince must additionally measure the torsional frequency, f_t. In order to do that, the machine's setup has to change completely. Following the standard *E1876–01* [34], the specimen is supported at the torsional nodal planes. This means it must be supported in its centre, specifically at the midpoint of its length and width, as illustrated in Figure 2.14.

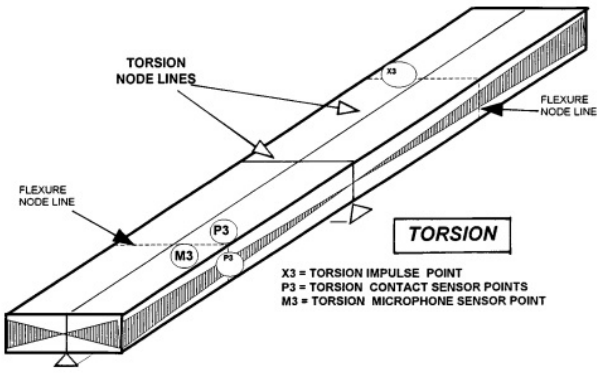

Figure 2.14: Rectangular specimen tested for torsional vibration [34]

In the case of the evaluation of the torsional frequency, the transducer is positioned at 0.224 of the length of the specimen, in highlighted position M3 (Fig.

2.14), which is a flexural nodal point. The impulser is located at the opposite quadrant with respect to the microphone, again in the flexural nodal point (point X3 in Figure 2.14).

The microphone picks up the fundamental flexural and torsional frequencies in order to calculate all three material properties.
For the elastic modulus, the machine uses the equation shown in paragraph 2.1 (eq. 2.1).
For the shear modulus G, it exploits the following equation:

$$G = \frac{4Lmf_t^2}{bt}\left[\frac{B}{(1+A)}\right] \tag{2.4}$$

Where f_t is the fundamental resonant torsional frequency and A and B are correction factors, calculated respectively with equations 2.5 and 2.6:

$$A = \frac{[0.5062 - 0.8776(\frac{b}{t}) + 0.3504(\frac{b}{t})^2 - 0.0078(\frac{b}{t})^3]}{12.03(\frac{b}{t}) + 9.892(\frac{b}{t})^2} \tag{2.5}$$

$$B = \left[\frac{\frac{b}{t} + \frac{t}{b}}{4(\frac{t}{b}) - 2.52(\frac{t}{b})^2 + 0.21(\frac{t}{b})^6}\right] \tag{2.6}$$

These correction factors depend on the geometry of the test specimen. In particular, A (eq. 2.5) is a function of the ratio of the beam's width (b) to its thickness (t).

With the values of E and G obtained, it is possible to calculate the Poisson ratio with this simple correlation:

$$\mu = \left(\frac{E}{2G}\right) - 1 \tag{2.7}$$

The results obtained with this set-up are presented in the next paragraphs..

2.2.1 Set-up

The machine used for the evaluation of the previously mentioned mechanical properties did not include the set-up described above. Therefore, the first objective

was to design a system similar to the one outlined earlier.

Rock wool was selected for the main structure, as it can withstand high temperatures without compromising its integrity. The scheme of the set-up is illustrated in figure 2.15.

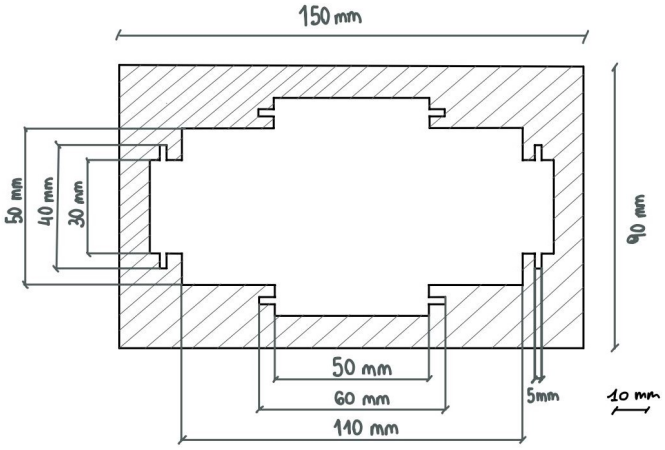

Figure 2.15: Initial scheme of the structure for the set-up of the E, G, μ

In the sections at the side, small cylinders of pure copper were used to then tensioning the wires in the configuration of figure 2.14. The CuCrZr specimen would be placed on top of the titanium cables. The materials mentioned were chosen to keep in mind the range of temperature at which they would be subjected during the test. All of them have high-temperature resistance.

Unfortunately, the first attempt was unsuccessful due to the support structure breaking when we tried to place the first copper cylinder for the support (Fig. 2.16).

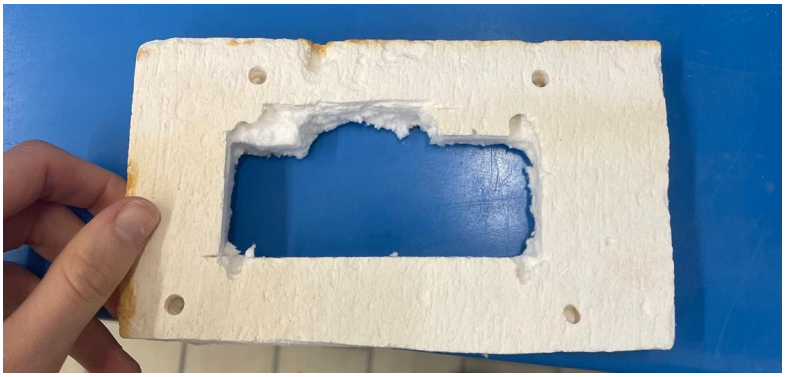

Figure 2.16: Broken structure for measurement of mechanical properties

The second attempt focused on the reinforcement of the supports on the side of the structure. he sections where the copper cylinders are positioned were made deeper into the rock wool compared to the first attempt. The final structure is depicted in Figure 2.17.

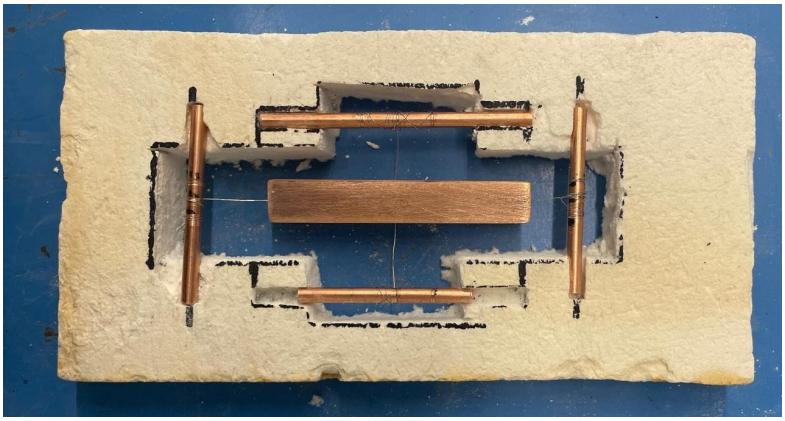

Figure 2.17: Structure used for the evaluation of mechanical properties

Indeed, the structure in Figure 2.17 was able to withstand the weight of the CuCrZr specimen. Two tests were conducted.

2.2.2 Results

For the evaluation of the Young modulus, the machine used the fundamental flexural resonant frequency (eq. 2.1). The behaviour of E as the temperature increases (Fig.2.18) is consistent with the tests run with the first set-up (2.11).

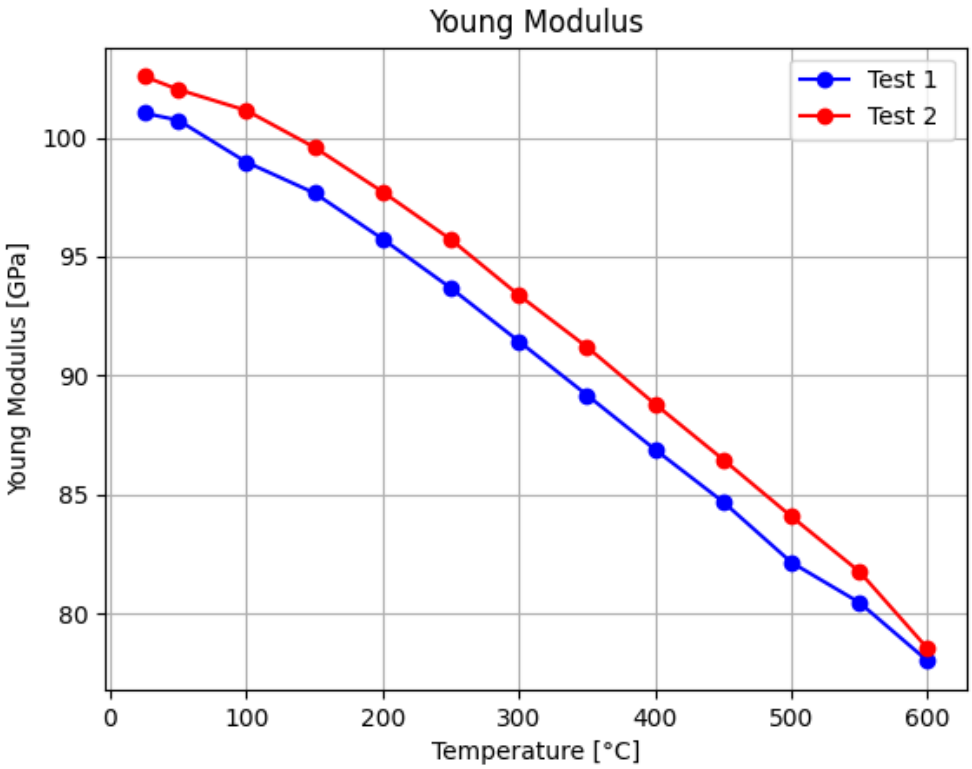

Figure 2.18: Elastic modulus in controlled atmosphere (Ar) with complete set-up

The calculation of the shear moduls employs the fundamental torsional resonant frequency (eq. 2.4).

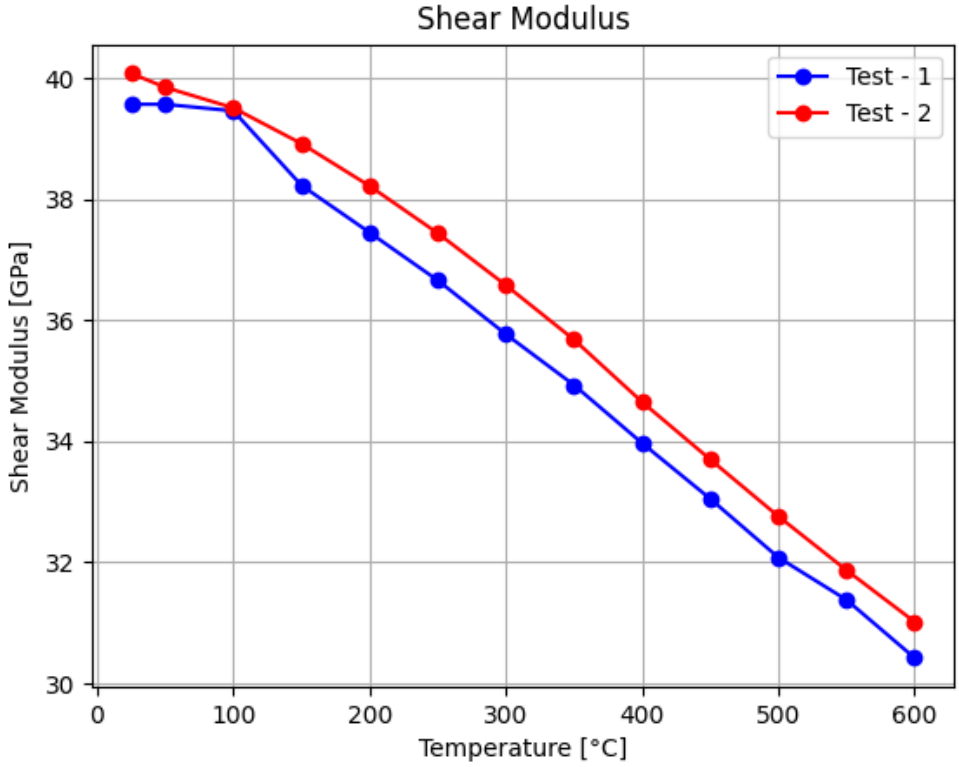

Figure 2.19: Shear modulus in controlled atmosphere (Ar) with complete set-up

The behaviour (Fig. 2.19) is congruent with the existing literature. As the temperature increases the shear modulus, G, is expected to decrease [37]. Similar to the behaviour of the elastic modulus, with the increase of temperature the specimen is subjected to a decrease of stiffness, making the material less resistant to shear deformation and resulting in a reduction of the shear modulus.

The Poisson ratio is calculated exploiting the values of the elastic modulus (Fig. 2.18) and the shear modulus (Fig. 2.19). The machine exploiting the equation 2.7 gives back the values shown in Figure 2.20.

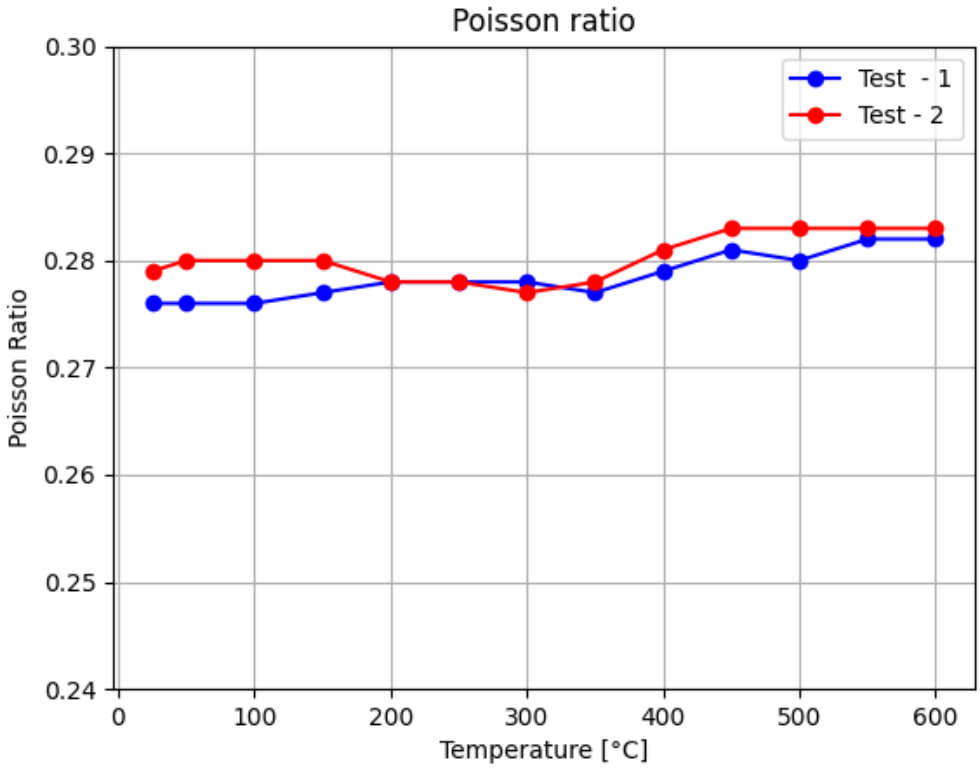

Figure 2.20: Poisson ratio in controlled atmosphere (Ar) with complete set-up

The behaviour is different in comparison of the one of the elastic modulus and shear modulus. The change in μ is a reflection of the corresponding changes in their values. As the temperature increases, μ increases too. As mentioned earlier, CuCrZr undergoes thermal expansion (par. 3), expanding in all directions. This results in a decrease in stiffness, making it easier for the material to deform laterally under the same axial stress, which in turn increases the transverse deformation. This increase in transverse deformation leads to a rise in the Poisson ratio.

Chapter 3

Thermo-mechanical analysis

3.1 Introduction

The thermo-physical analysis aims to define the thermo-physical characteristics of a material, describing how it responds to temperature changes. This section focuses on the coefficient of linear thermal expansion (CTE), an intrinsic property of materials [38]. The CTE quantifies how a material's size and volume change in response to temperature variations [39, 40].
The coefficient of linear thermal expansion, α_m, is defined as the relative expansion divided by the change in temperature. The relative expansion is the change in length (ΔL) over the initial length (L_o). Thus, α_m is calculated as:

$$\alpha_m = \frac{1}{L_o}\frac{L_2 - L_1}{T_2 - T_1} = \frac{1}{L_o}\frac{\Delta L}{\Delta T} \tag{3.1}$$

L_o is the length at the initial temperature, while L_1 and L_2 are the lenght respectively at temperature T_1 and T_2 (Fig. 3.1).

Figure 3.1: Schematic of the linear thermal expansion for a solid [38].

This measurement represents the slope of the chord between two points on the plot of length against temperature (Fig. 3.2. In this case, the CTE refers to a temperature range rather than a single temperature.
The true coefficient of linear expansion, on the other hand, is correlated to the derivative $\frac{dL}{dT}$ at a specific temperature [38]. It is calculated as:

$$\alpha = \frac{1}{L_o}\frac{dL}{dT} \tag{3.2}$$

This definition characterizes the coefficient of thermal expansion as the slope of the tangent on a plot of length versus temperature (Fig. 3.2).

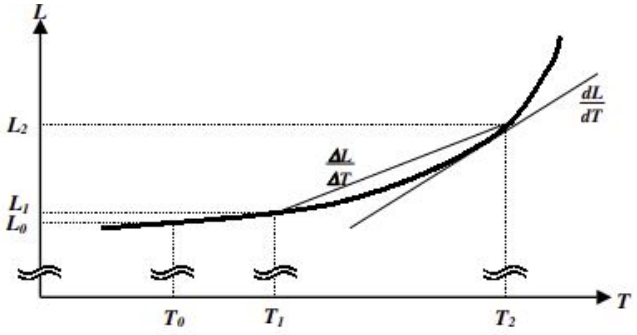

Figure 3.2: Change in length, L, of a sample of material as a function of temperature, T [39].

3.2 Set-up

The objective of this testing is to evaluate the CTE for the copper alloy, CuCrZr. To evaluate the aforementioned property, the dilatometer *DIL 402 PC* from NETZSCH was used.

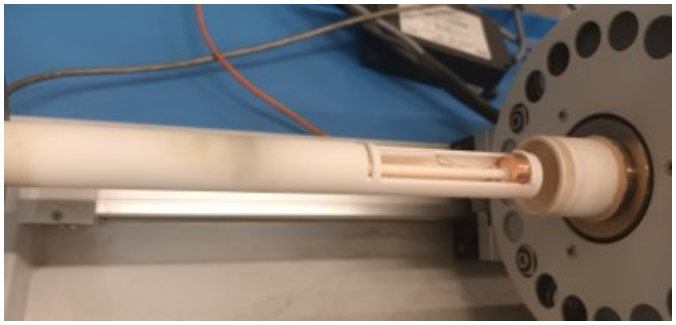

Figure 3.3: Pushrod dilatometer used for the evaluation of CTE

The instrument used for this measurement is a pushrod dilatometer, which detects the dimensional changes as the specimen undergoes a controlled temperature program. As shown in Figure 3.3, the sample is placed between the pushrod and the sample holder. Temperature-induced positional shifts are detected through a linear variable displacement transducer unit, which collects information from the pushrod's movement [38]. The machine outputs a file containing the relative expansion ($\frac{dL}{L_o}$) as a function of the temperature.
In this case, a CuCrZr cylinder of 5 mm of thickness (Fig. 3.4) was used to measure the CTE values from RT up to 600°C.

Figure 3.4: CuCrZr specimen used for the CTE measurement

The tests were performed in controlled atmsphere (Argon) in order to minimize the influence of the oxidized layer.

3.3 Results

The test was conducted three times on the same specimen of CuCrZr shown in Figure 3.4.
As described in the *set-up* section (par. 3.2), the machine outputs a file containing relative expansion as a function of the temperature. The results obtained from the three tests performed are shown in the following plot (Fig.3.5). Since the same sample undergoes heating from RT up to 600°C, it experiences irreversible changes, such as grain growth. Consequently, slight variations in the results across the three tests are expected.

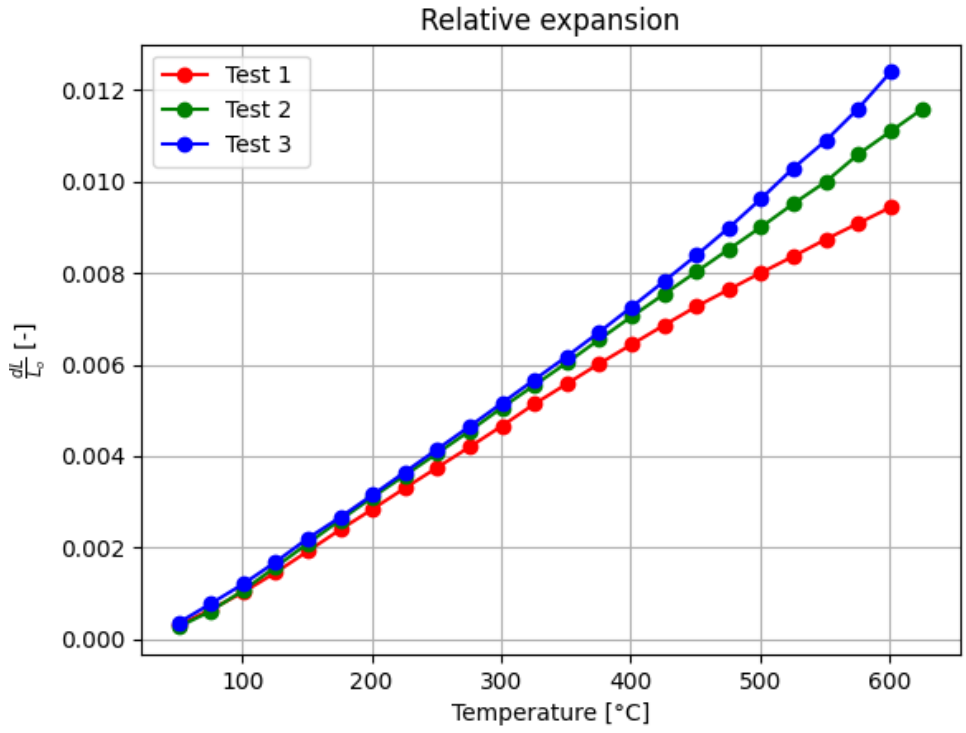

Figure 3.5: Relative expansion

The graph of the relative expansion (Fig. 3.5) clearly shows that, after the first test, the sample underwent an irreversible elongation, as evident from the shift in the second curve. Similarly, the difference between the second and third curves highlights further changes in the specimen following the second test. To better evaluate the difference among the results from the test, it is useful to look at the standard deviation (Fig. 3.6).

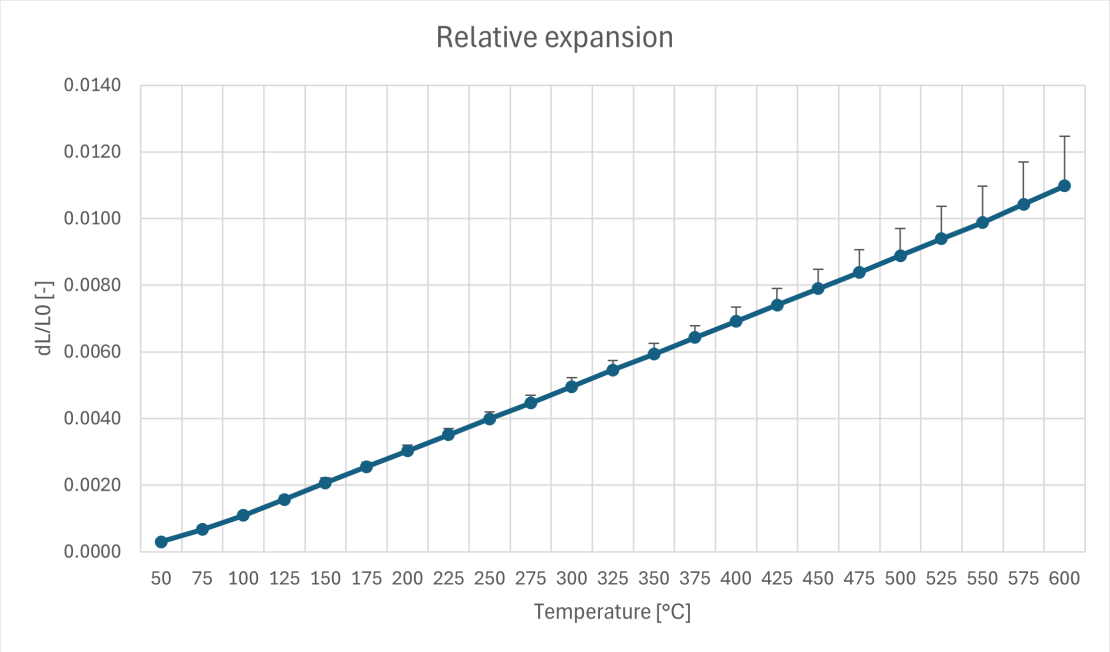

Figure 3.6: Standard deviation of linear expansion

The maximum value of standard deviation observed is 0.0015, corresponding to the measurement at 600°C. The coefficient of variation related to this value is 13.51%, indicating a significant deviation from the average. However, it is important to emphasize again that the same CuCrZr sample was reused across tests, which may have influenced the results.
Furthermore, using equation 3.2, the coefficient of thermal expansion α was calculated. The results for the three tests are shown in the following plot.

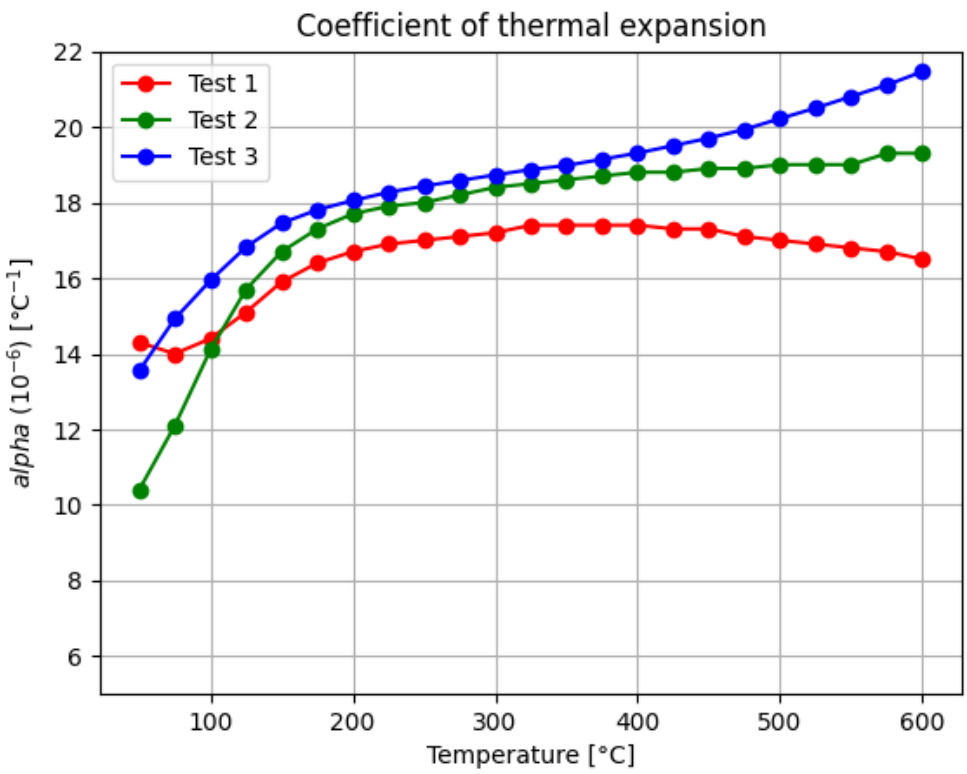

Figure 3.7: Coefficient of thermal expansion

It is also evident from Graph 3.7 that using the same CuCrZr sample across tests affected the results, with the greatest differences occurring at the ends of the curves. This trend is also apparent in the plot of the standard deviation (Fig. 3.8).

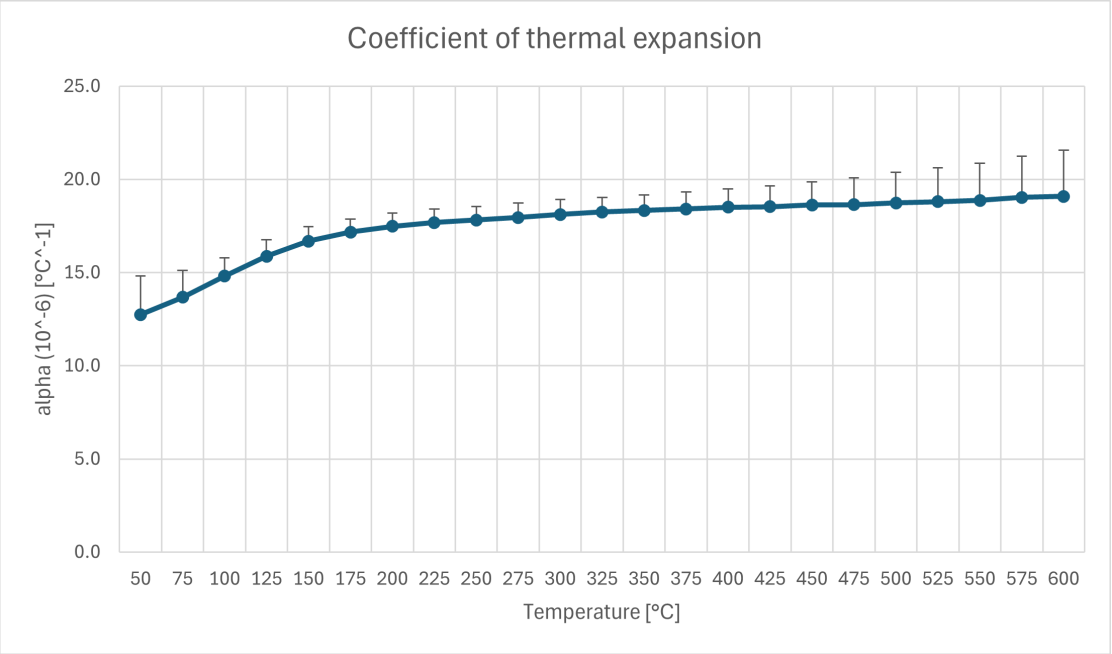

Figure 3.8: Standard devoefficient of thermal expansion

The standard devation is high along the entire curve, with the peak at 600°C showing a standard deviation of 2.49, corresponding to a coefficient of variation of 13.04%, which is notably high. To verify reproducibility, it is essential to repeat the measurements on different specimens to minimize the influence of prior heat treatments on the sample.

Chapter 4

Necking

4.1 Introduction

The necking and the radius of curvature of a specimen are evaluated through tensile testing.
Necking is a mode of tensile deformation in which strain is localized in a small region of the specimen. As a result, the cross-sectional area of the material decreases more rapidly, becoming the point with the highest local stress. Once necking begins, the distribution of the stress and strain in the specimen becomes complex. Consequently, the engineering stress-strain curve obtained from a standard tensile test, after the necking phenomenon, only provides an average stress-average strain relationship. Analyzing the stress applied in the necking region gives a better understanding of the true stress-strain relationship [41].

To track the evolution of the necking throughout the tensile test, a Python program was written in order to post-process the images obtained during measurements. The script is adapted for each test due to the different characteristics of the frames captured during different experiments.
The measurements were expected to be performed on IG-CuCrZr, as the mechanical

and thermo-mechanical tests (ch. 2, ch. 3).
However, to first establish a method to track the evolution of the diameter, preliminary tests were conducted on a specimen of pure copper with the geometry outlined below (Fig. 4.1). The only difference between the sketch and the actual specimen is the diameter. Instead of 4 mm, the actual diameter of the specimen was 5 mm, as specimens with a 4 mm diameter could not be produced.

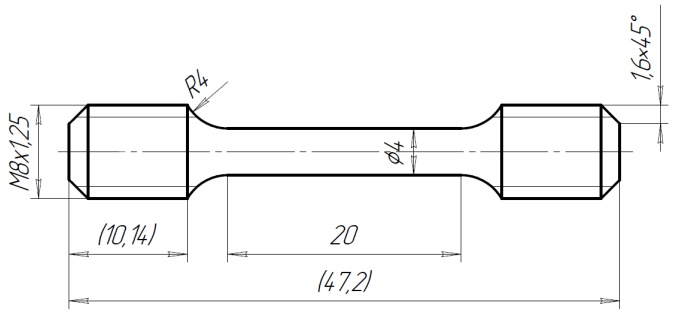

Figure 4.1: Geometry of cylinder specimen

The tensile test was performed at J-Tech laboratory in Politecnico di Torino using the Zwick-Roel *50kN Allround table-top*, equipped with the LaserXTens. The tensile tests were performed at RT and at 600°C with a strain rate of 0.5 $\frac{mm}{min}$.

4.2 Test one

A copper specimen with the geometry mentioned above (Fig. 4.1) was used. The test was successfull as the frames (Fig. 4.2) were correctly obtained.

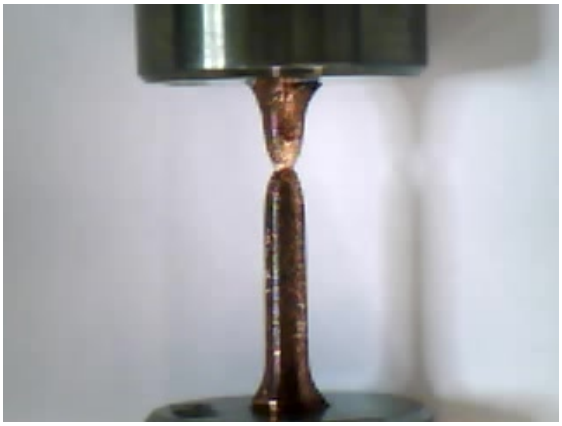

Figure 4.2: Frame example taken during the testing

The test was conducted at RT in air. An USB camera was used to capture the frames during the test. To enhance the contrast between the specimen and the background, a white piece of paper was placed behind the sample.
The initial post-processing analysis started with these frames. A Python script was developed to analyze the change in diameter from the start of the test until failure of the specimen. The first step was to improve the image quality. At first, a Gaussian blur filter was applied to reduce noise in images taken under low lighting conditions. Next, a sharpening filter was used to enhance image clarity making the edge of the specimen more distinct. After these filters were applied, the background was removed through another Python script. This was a crucial passage for the analysis, as it enabled the next step of isolating the specimen's clean edges. Employing the library *skimage* in Python, the *Canny* edge-detection feature was used to extract the specimen's boundaries (Fig. 4.3).

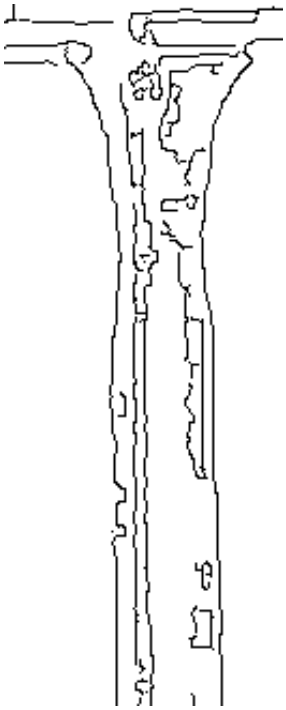

Figure 4.3: Edges extrapolated by Python script

The resulting images (Fig. 4.3) were cropped to focus on the necking region. In this area, the exact point where the diameter reduction begins was identified. A vertical line passing through this specific point was drawn on each side of the specimen and the distance between these two lines provided the change in diameter. This method allows for plotting the diameter change as a function of the frames. However, in this case, this analysis was not achievable. The reasons lay on the poor image quality and the specimen's surface condition. As shown in Figure 4.2, the specimen surface had some imperfections that caused the edge extrapolation to not be effective.

Consequently, the program was unable to accurately track the changes at the necking initiation point, making it impossible to calculate the diameter change (Fig. 4.4).

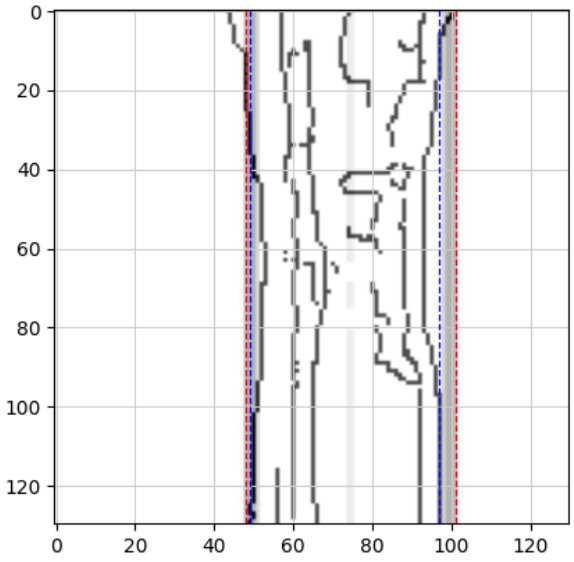

Figure 4.4: Failed edges extrapolated by Python script

For the following test at RT (par. 4.3), greater attention was given to the surface finish of the specimen in order to enable the script to accurately detect its edges.

4.3 Test two

The geometry of the specimen used for this measurement corresponds to the one described in Figure 4.1. As before, the diameter of the specimen is 5.
The set-up (Fig. 4.5) is the same as the one conducted in the first test (par. 4.2).

Figure 4.5: Set-up of test one

Once again, a piece of white paper was positioned behind the specimen in order to enhance the contrast between the sample and the background. Additionally, a light source was positioned in front of the machine to improve the definition of the specimen's surface. This setup helped to homogenize the lighting and obtain frames with higher resolution. (Fig. 4.6).

Figure 4.6: Frame example taken during testing

Compared to the frames captured during the first test (Fig. 4.2), these new ones are noticeably cleaner.
The frames were analysed using the same Python script described in the *Test one* paragraph (par. 4.2). In this case, thanks to the higher resolution, the script was able to more precisely track changes in the diameter.

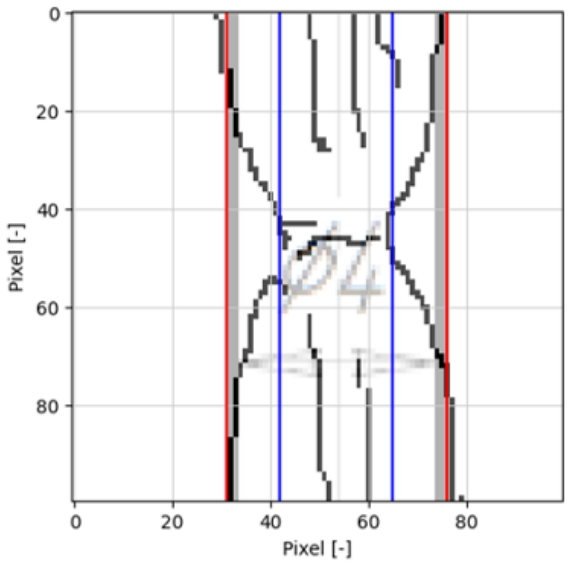

Figure 4.7: Specimen's diameter during RT testing

It was then possible to plot the change in diameter as function of the number of frame. The resulting graph (Fig. 4.8) highlights errors in certain frames.

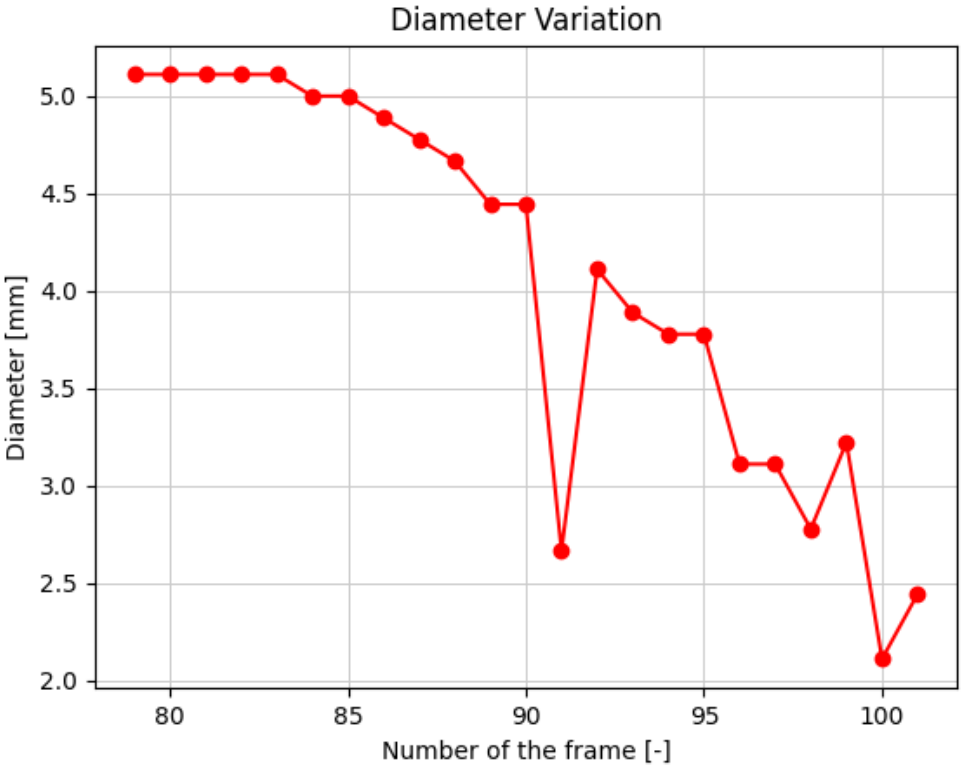

Figure 4.8: Diameter as a function of the frame number

The x-coordinate (number of frame) starts at 79, which corresponds to the beginning of the necking phenomenon.
It is important to notice that at certain points of the analysis, the script fails to accurately track the diameter change (e.g., frame 91). To achieve a more continuous representation of diameter change, a third-degree polynomial fit was applied (Fig. 4.9).

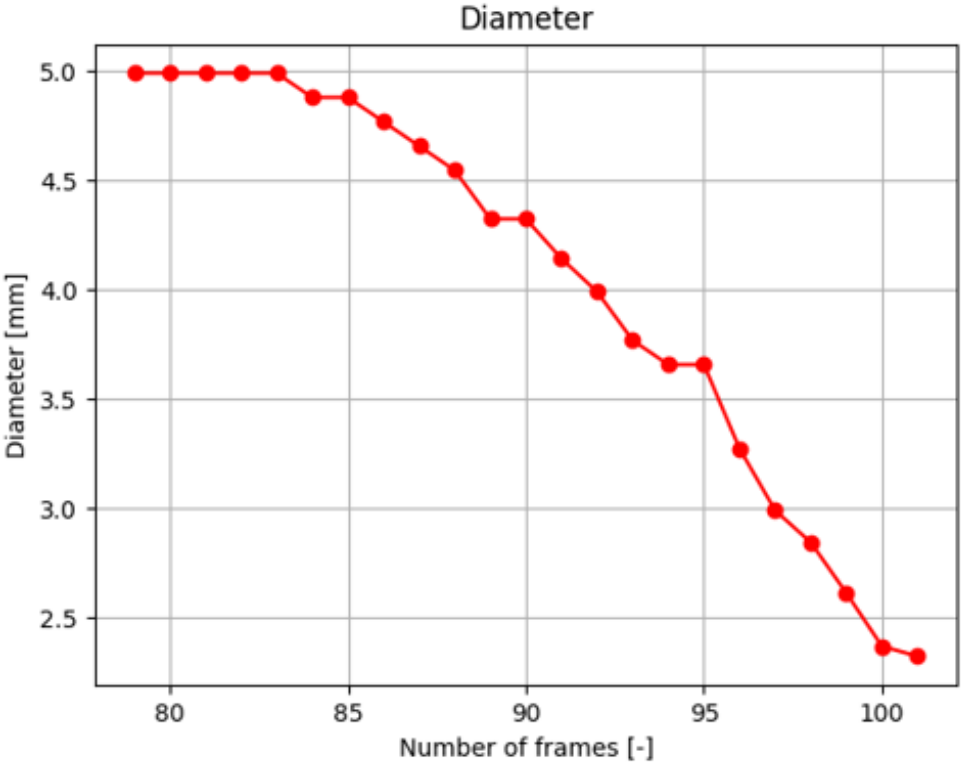

Figure 4.9: Diameter as a function of the frame number

However, it was not possible to plot the diameter change as a function of the applied stress, as there was no synchronized parameter to align the two variables. The USB camera used for capturing frames was not synchronized with the force measurement program. To address this in subsequent tests, frames were captured using LaserXTens instead of an external USB camera. (par. 4.4, 4.5).

4.4 Test three

The specimen used for test three follows the standard geometry (Fig. 4.1). The test was performed at 600°C. The machine used was the one used for the previous measurements with the addition of an oven to achieve the required temperature.

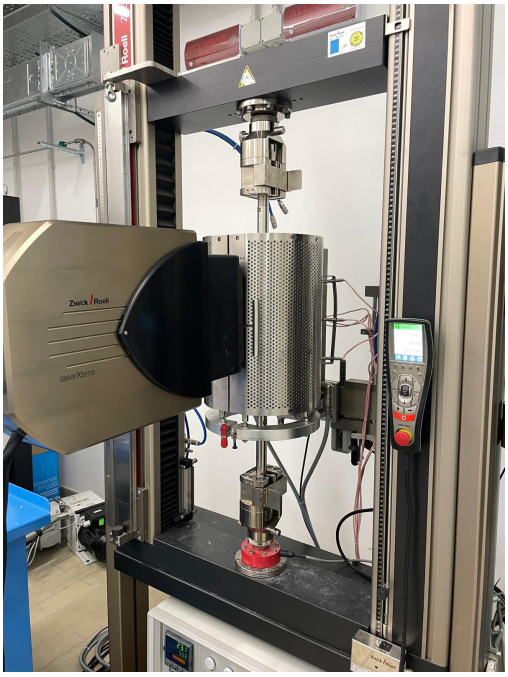

Figure 4.10: Set-up for high temperature testing

The test was executed in controlled atmosphere using argon (Ar) to minimize the influence of the oxidized layer on the test results. To ensure proper insulation and maintain a complete argon atmosphere, rock wool was used to cover the uncovered sections of the oven. Additionally, a more concentrated flow of argon was directed toward the specimen, facilitated by the tool shown in figure 4.11.

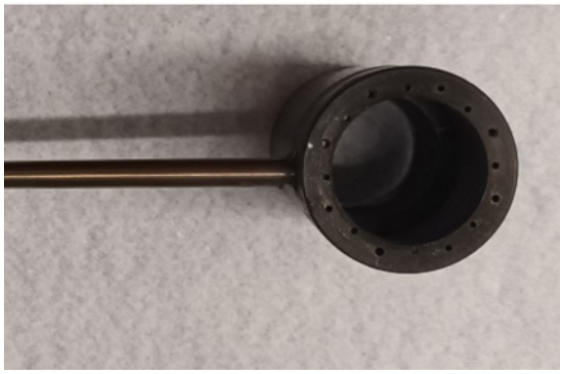

Figure 4.11: Tool for the Ar flow

The camera used for test three was the LaserXTens. It was chosen beacuse it was the only way to capture clear images of the specimen inside the oven at high temperature without causing damage. By adjusting the laser set-up parameters, good-quality images (Fig. 4.12) were obtained throughout the tensile test.

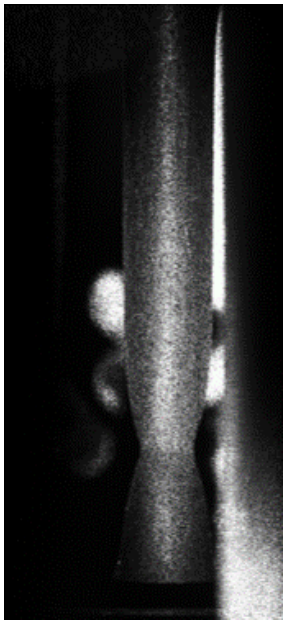

Figure 4.12: Frame during test with laser

However, the Python script used for the previous measurements at RT was no longer suitable for these frames.

This time, only a sharpening filter was applied to the images. The Gaussian blur was omitted, as it increased the noise level, which was counterproductive. Moreover, the background of the image was not removed anymore, as the program struggled to accurately remove it without cutting into the specimen. Instead, the image colors was inverted to to enhance the edge of the specimen. Using this modified image, the previously described process was repeated to identify the point where necking begins. From this information, a vertical line was drawn on both sides of the specimen (Fig. 4.13), highlighting the change in diameter.

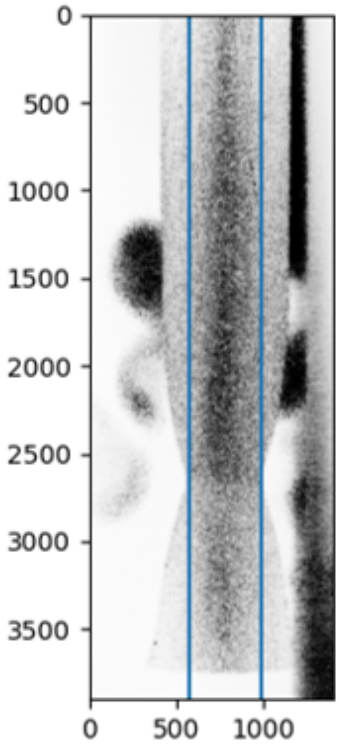

Figure 4.13: Specimen's diameter at 600°C captured by LaserXTens

From this analysis, it was possible to obtain a plot of the change in diameter as a function of the number of frames.

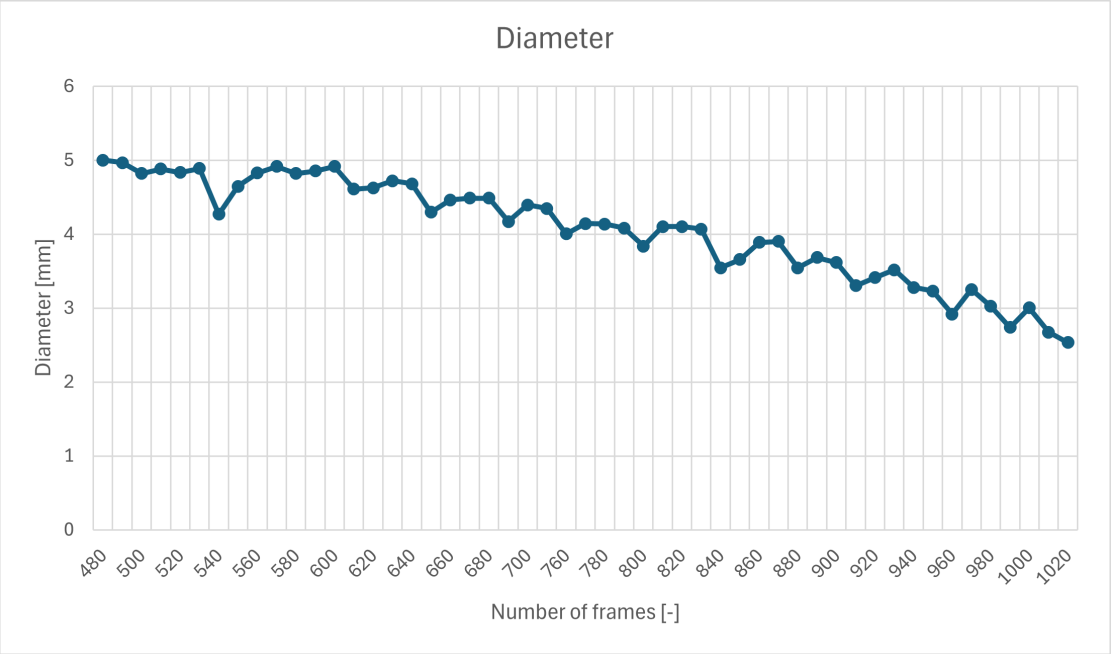

Figure 4.14: Change of specimen's diameter at 600°C

There is an important aspect related to this type of test: it is known that the laser captures two frames per second. By knowing the total number of images captured throughout the test, it is possible to correlate the frame number with the time at which the image was taken. By doing this and fitting a third-degree polynomial, as was done in test two (par. 4.3), it is possible to obtain a continuous representation of the decrease in diameter as a function of the time (Fig. 4.15).

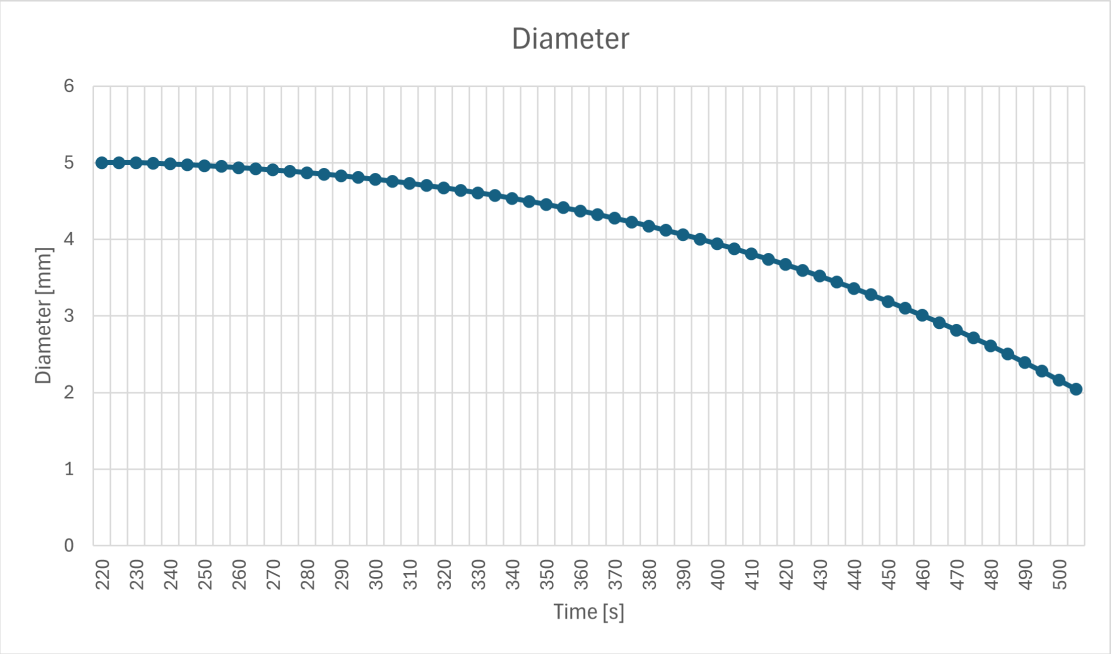

Figure 4.15: Change of specimen's diameter at 600°C as function of time

Furthermore, the software used for the tensile test outputs a file with the force applied to the specimen versus time. To calculate the true stress applied on the specimen, the following equation is used:

$$\sigma = \frac{F}{A} \tag{4.1}$$

Where F is the force applied and A is the cross-sectional area over which the force is applied. As the necking begins, the diamter decreases, leading to a reduction in area A.

With the true stress calculated, its value as a function of time can be determined. By correlating this with the time associated with the number of frame, a common parameter—time—emerges between the true stress and the change in diameter. This allows for the generation of a plot depicting the change in diameter as a function of true stress (Fig. 4.16).

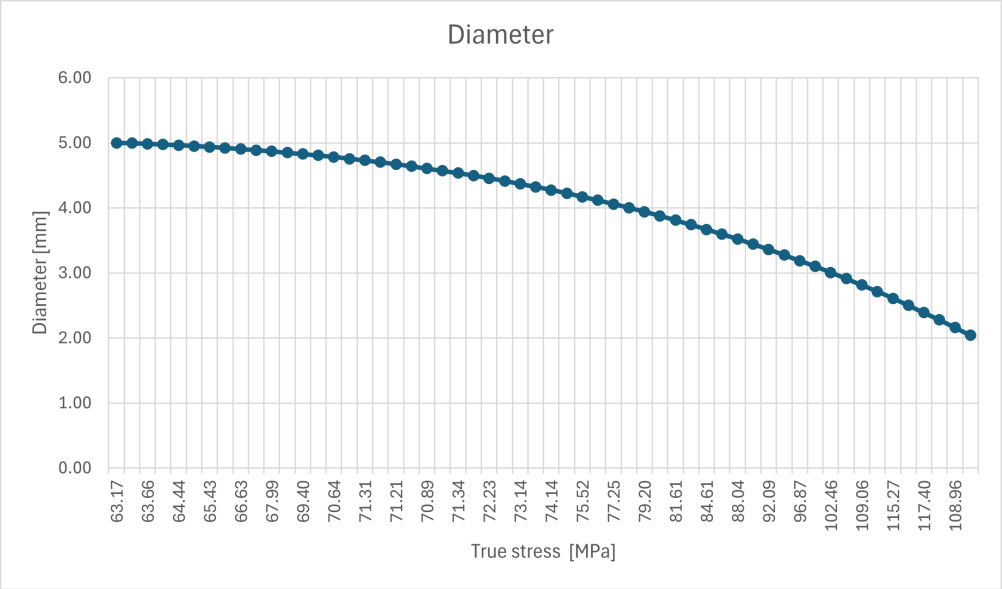

Figure 4.16: Change of specimen's diameter at 600°C as function of true stress

The complete evolution of the diameter over the strain is illustrated in Figure 4.17.

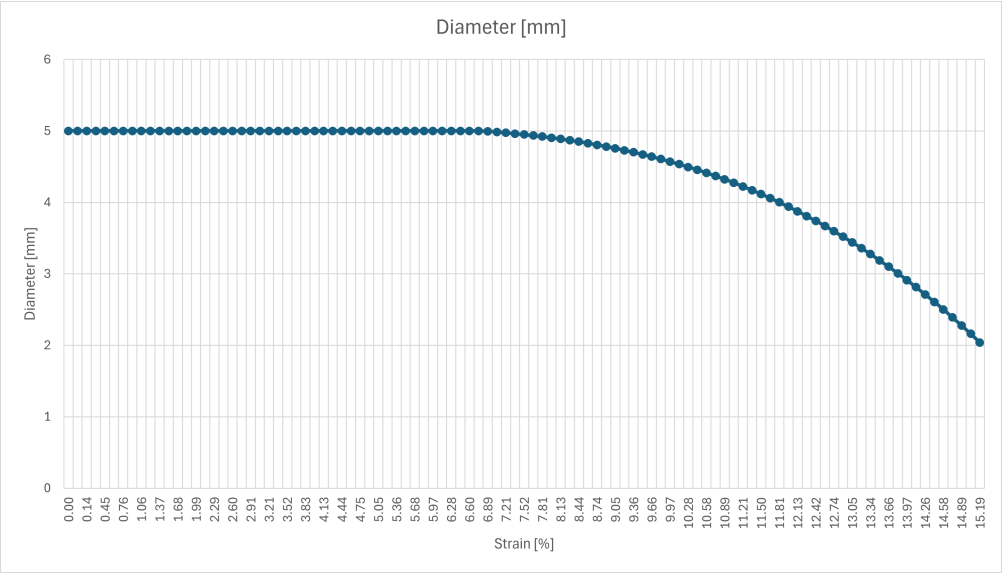

Figure 4.17: Change of specimen's diameter at 600°C as function of strain

By knowing the complete evolution of the diameter, and thus the evolution of

true stress—throughout the tensile test, it becomes possible to derive the true stress-strain curve of the specimen.

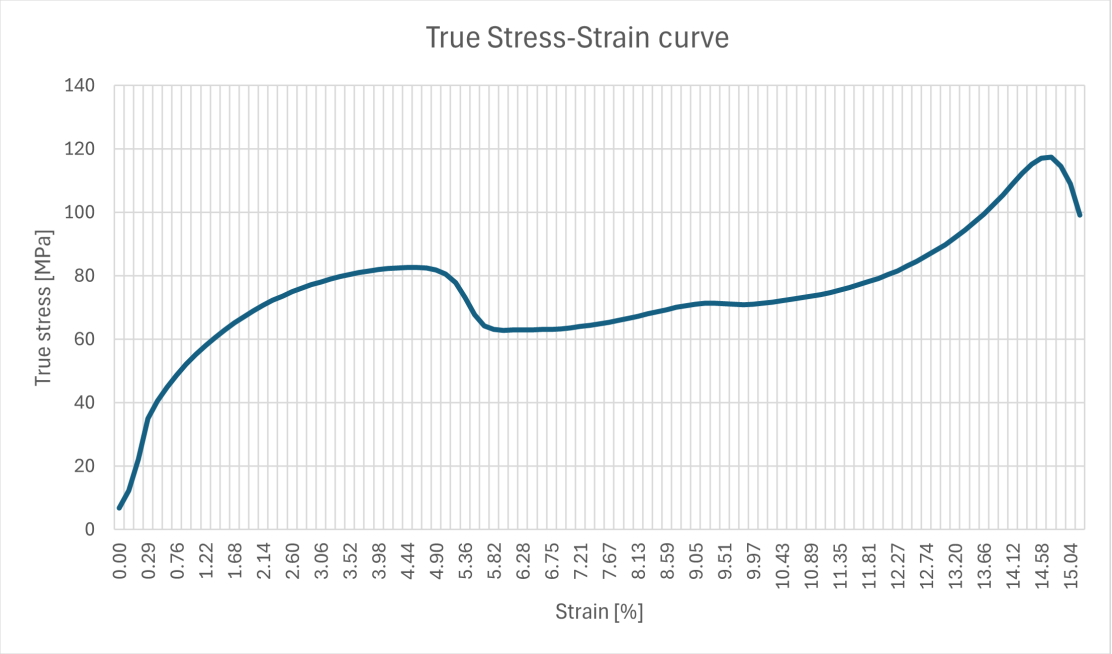

Figure 4.18: True stress-strain curve of test three at 600°C

One of the most interesting aspect revealed by this analysis can be observed in the engineering stress-strain curve. The stress reaches a maximum at a strain of 4.90%, corresponding to a stress of 82.44 MPa. After this peak, there is a sudden decrease in the applied stress.

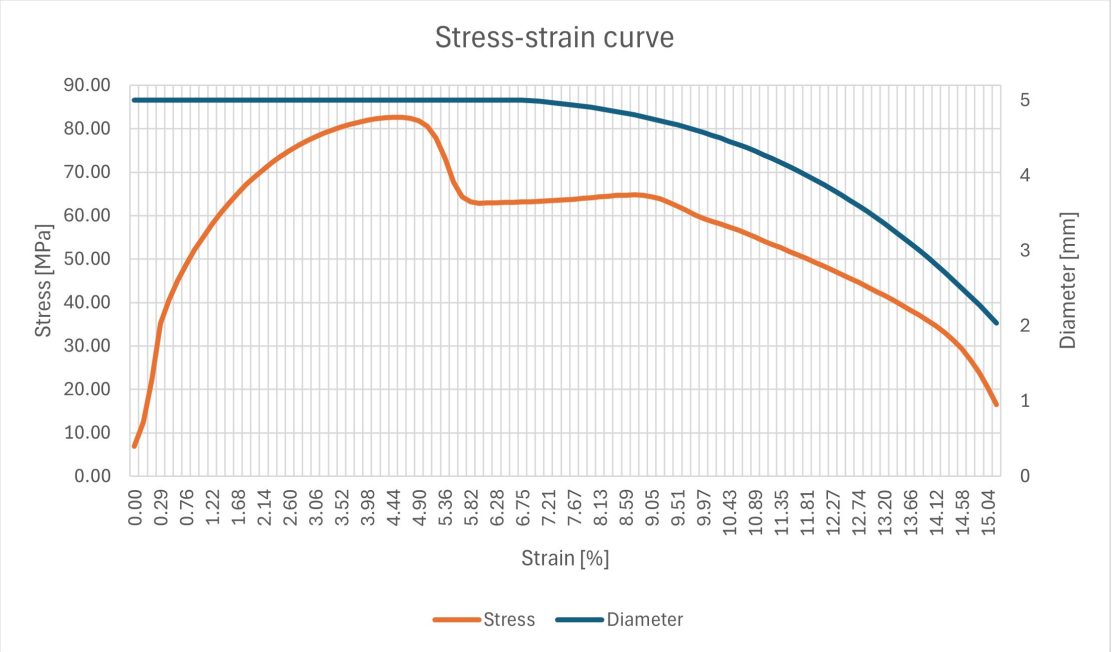

Figure 4.19: Stress-strain curve at 600°C

A possible explanation for this behavior is that, as the force applied to the specimen continuously increases, the diameter decreases as necking begins. While the stress in the necking area increases, the force applied along the entire length of the specimen decreases. Since stress is calculated using equation 4.1 with area A based on the initial diameter (5 mm), this results in an apparent reduction in stress. However, as shown in Graph 4.19, this reduction in diameter does not immediately align with the corresponding strain. Instead, after reaching a stress of 62.89 MPa, there is a slight increase in applied stress until it reaches the strain at the onset of necking (6.75%).

This behaviour is attributed to the Dynamic Recrystallization (DRX) phenomenon. DRX is a phenomenon that occurs during hot deformation. In this case, the specific

type of DRX is dynamic discontinuous recrystallization (DDRX), which involves the nucleation of new grains at the expense of regions that are highly dislocated [42]. The stress-strain response of a specimen undergoing this phenomenon is characterized by a curve with one or multiple peaks (Fig. 4.20), depending on factors such as temperature (T), strain rate ($\dot{\epsilon}$), and initial grain size.

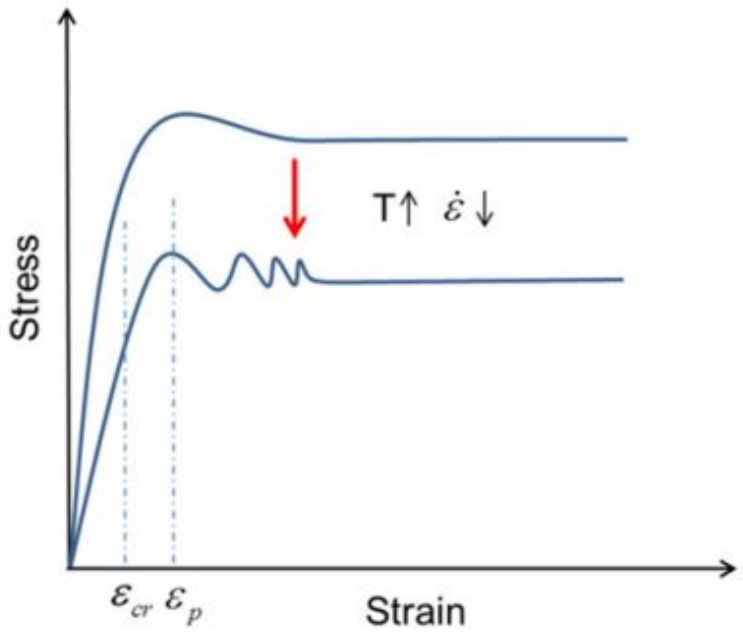

Figure 4.20: Observed experimental characteristics of DDRX with changes in deformation conditions [42].

4.5 Test four

The fourth tensile test conducted on a copper specimen (Fig. 4.1) was performed at RT, similar to the test described in paragraph 4.3. It was not necessary to work in controlled atmosphere, as oxidation reactions do not occur at 25°C; these reactions happen only at elevated temperatures.

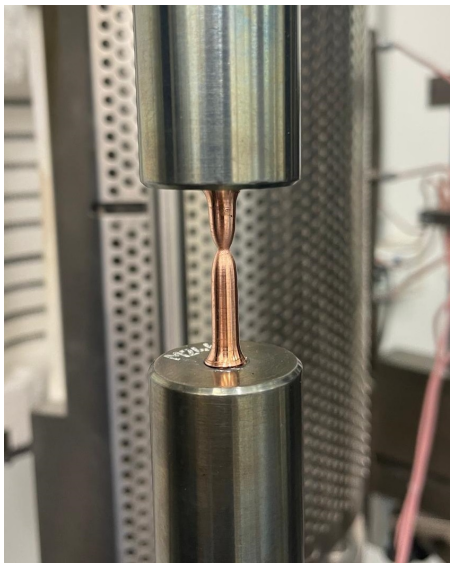

Figure 4.21: Specimen after test at RT

Instead of using the USB camera, the LaserXTens was utilized, as in test three (par. 4.4). This approach allowed for the verification of the script used for the high-temperature test. The frames obtained were of good quality. In comparison with the frames obtained from the test at 600°C (Fig. 4.12), the quality of the current frame is higher, but the contrast against the background is lower. For this reason, some modifications were made to the original script.

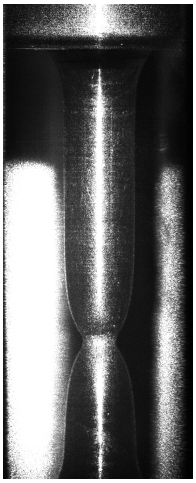

Figure 4.22: Frame from RT-test

The same filters used in the test three were applied. However, instead of inverting the color, the background was removed. This step was possible thanks to the higher quality of the frames. By selecting the color values of the background, a mask was created in order to isolate the specimen. With this extra step, it was possible to track the change in diameter (Fig. 4.23).

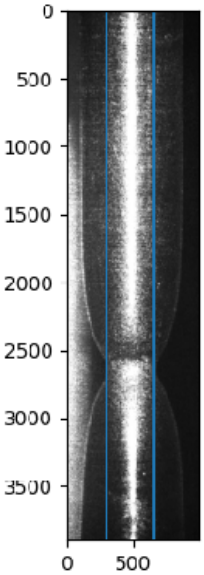

Figure 4.23: Specimen's diameter at RT captured by LaserXTens

Starting the analysis from the frame corresponding to the onset of the necking, the change in diameter as a function of time was obtained.

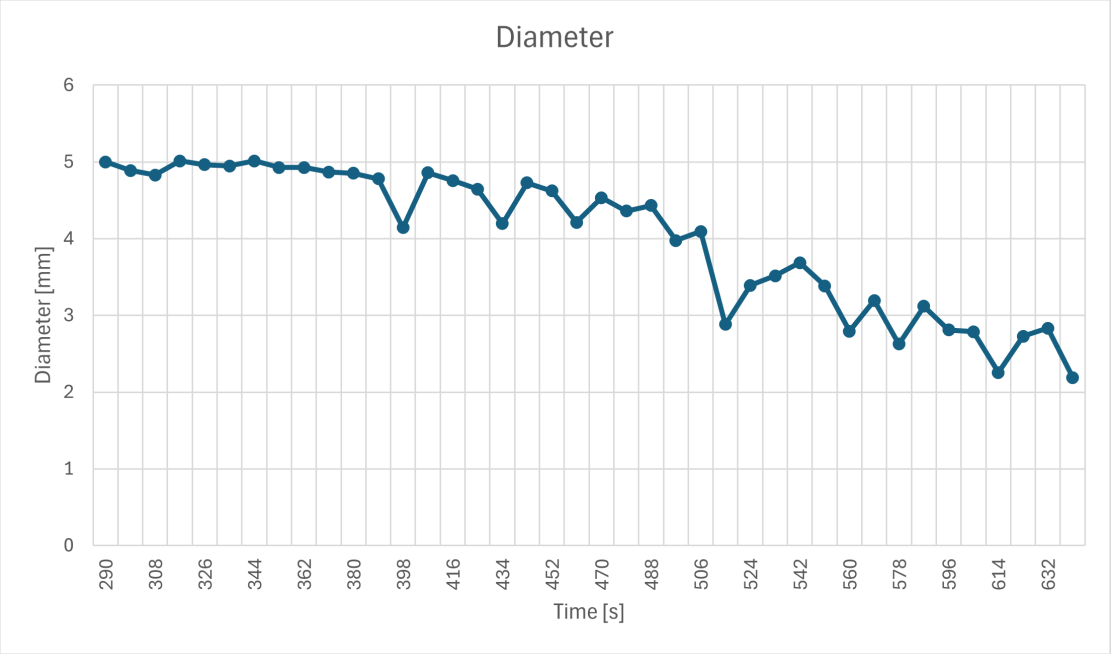

Figure 4.24: Change of specimen's diameter at RT

A third-degree polynomial was fitted in order to provide a continuous representation of the diameter change over time. Furthermore, since the test was performed as test three (par. 4.4), the same variable, time, was used to link the force applied to the diamenter's change. By knowing the force, applying equation 4.1, the true stress was calculated, with A representing the changing area. Consequently, the plot of the changing diameter as a function of true stress was generated.

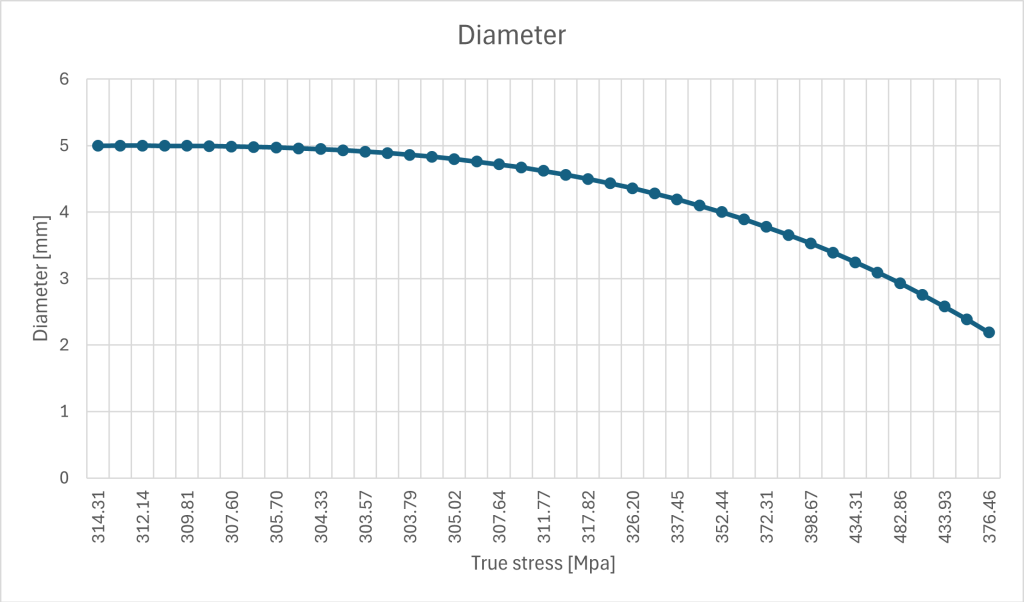

Figure 4.25: Diameter's change at RT as a function of true stress

Observing the complete evolution of the diameter (Fig. 4.26), it is evident that the necking begins at a strain of 4.15%.

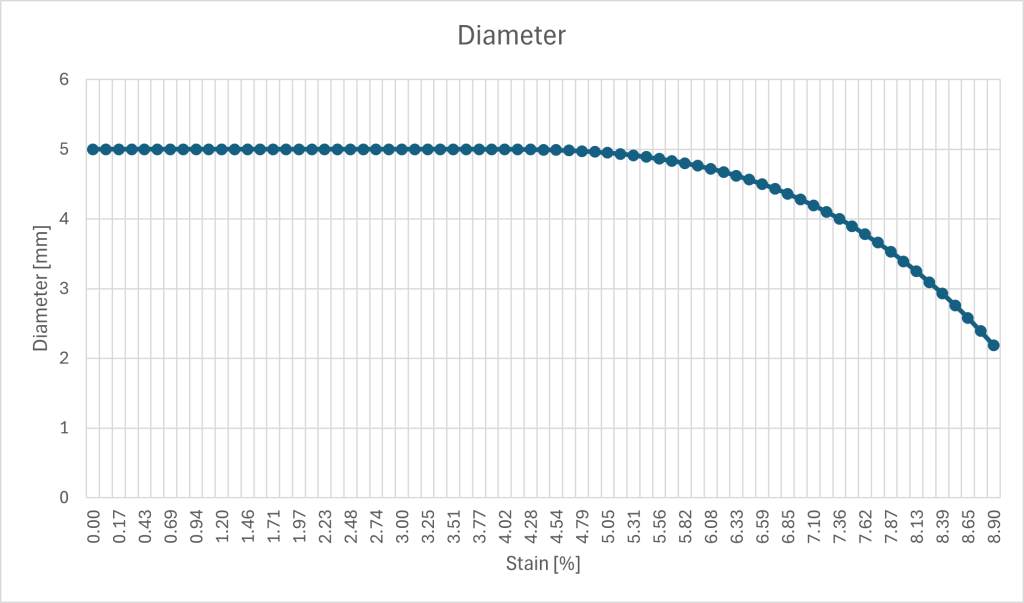

Figure 4.26: Diameter's change at RT as a function of strain

With the complete evolution of the diameter and, consequently, of the true stress, the true stress-strain curve can be obtained.

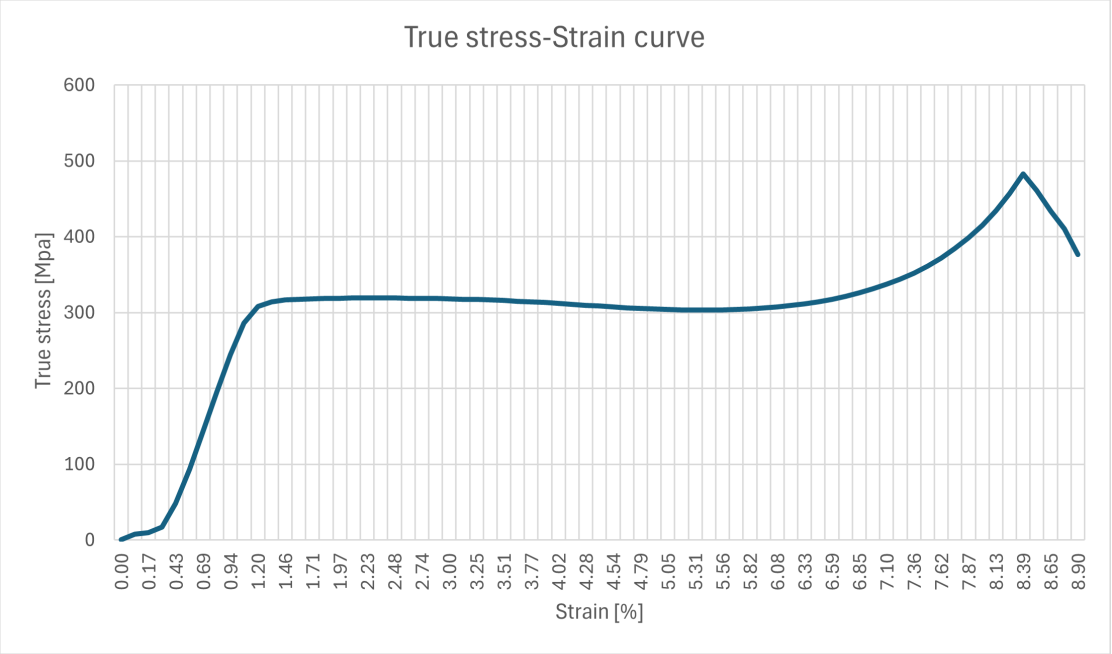

Figure 4.27: True stress-strain curve of test four at RT

4.6 Comparison between test three and test four

It's interesting to observe how the specimen of the same geometry behaves when it undergoes a tensile test at 600°C (par. 4.4) compared to RT (par. 4.5). The geometric characteristics of the two specimens after testing are shown in Table 4.1.

Table 4.1: Comparison of the geometry after test at 600°C and RT

Temperature	Necking [mm]	Diameter [mm]	Length [mm]
RT	2.19	4.88	31
600°C	2.98	4.26	36

It might be expected that, after the test at 600°C the diameter in the necking area would be smaller due to the increased ductility of the material at elevated temperatures. However, as shown in Table 4.1, the diameter after the test at RT is actually smaller. This behavior can be attributed to the material's enhanced ductility at high temperature, causing a more uniform reduction in diameter along the entire length of the specimen, as illustrated in Figure 4.28.

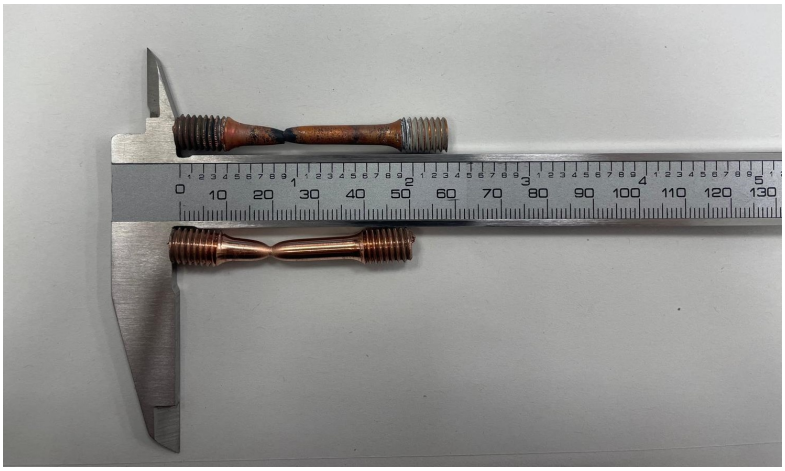

Figure 4.28: Difference in geometry after test at 600°C and RT

Indeed, by analyzing the engineering stress-strain curve of both tests together (Fig. 4.29), it can be observed that the specimen that was tested at 600°C undergoes greater strain. Consequently, the reduction in diamter is distributed along the

entire length of the specimen. In contrast, at RT, due to the lower ductility of the specimen, the reduction of the diameter is more concentrated in the necking area.

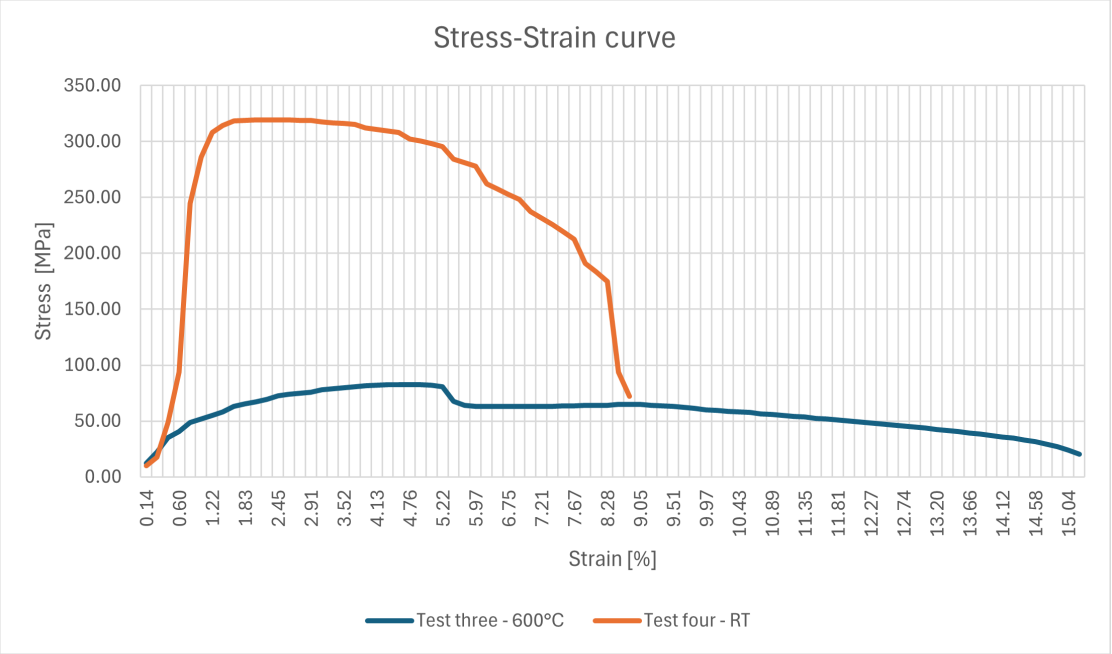

Figure 4.29: Stress-strain curve of the two tests

Another aspect to highlight from the stress-strain curve (Fig. 4.29) is the difference in the stress range applied to the specimens. To reach the same strain, the sample tested at 600°C is subjected to a stress ten times lower than that of the sample at RT. For a strain of 3.98%, the stress values are respectively 81.49 MPa and 312.10 MPa. This behaviour reflects the change of ductility at higher temperatures. As ductility, which is the ability of a material to undergo permanent deformation [43], increases, the material requires less applied force to achieve the same elongation. Consequently, the sample tested at 600°C reaches failure at a higher strain value compared to the strain at failure for the RT test.

4.7 Test five

In order to verify the reproducibility of the tests at high temperature using the method described in paragraph 4.4, another measurement was conducted at 600°C. The test was again performed in controlled atmosphere to minimize the influence of the oxidized layer. However, a thin layer of oxidation can still be observed (Fig. 4.30).

Figure 4.30: Specimen after test at 600°C

Once again, the LaserXTens was used to capture frames during the tensile test. The laser parameters were carefully controlled to achieve the highest possible resolution. The only minor issue was with the camera positioning.

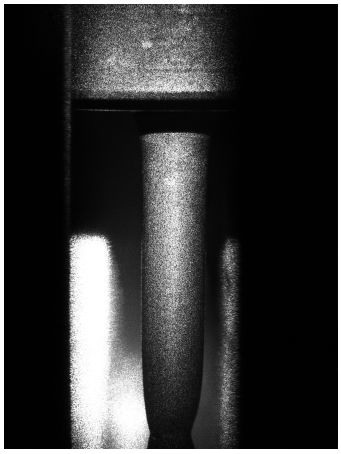

Figure 4.31: Frame obtained from the october test at 600°C

As shown in figure 4.31, necking is at the very bottom of the picture rather than centered, as in the frames captured during the previous tests. Nevertheless, using the same Python script as in the previous measurements, it was still possible to track the evolution of the diameter. The resulting plot of the diameter change over time is shown in the following graph.

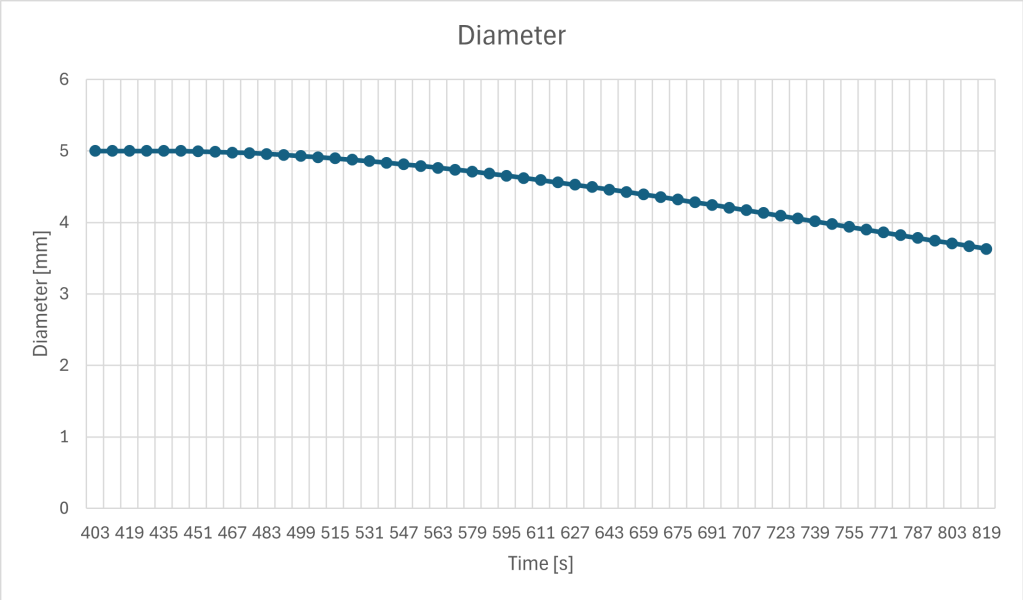

Figure 4.32: Diameter's change as a function of time

Similarly, using the same procedure described in paragraph 4.4 and utilizing the common time parameter between the captured frames and the machine results, it was possible to obtain the diameter as a function of true stress (Fig. 4.33).

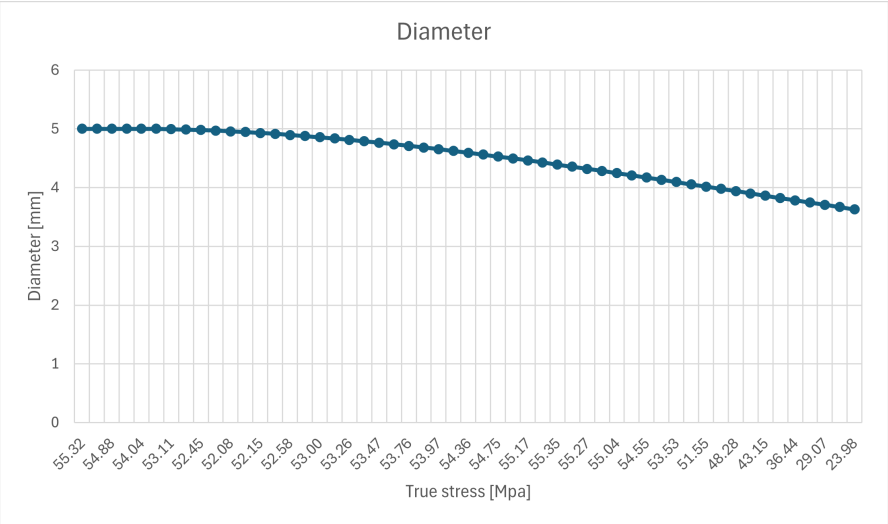

Figure 4.33: Diameter's change as a function of true stress

The complete evolution of the diameter over the strain of the specimen is shown in the following plot.

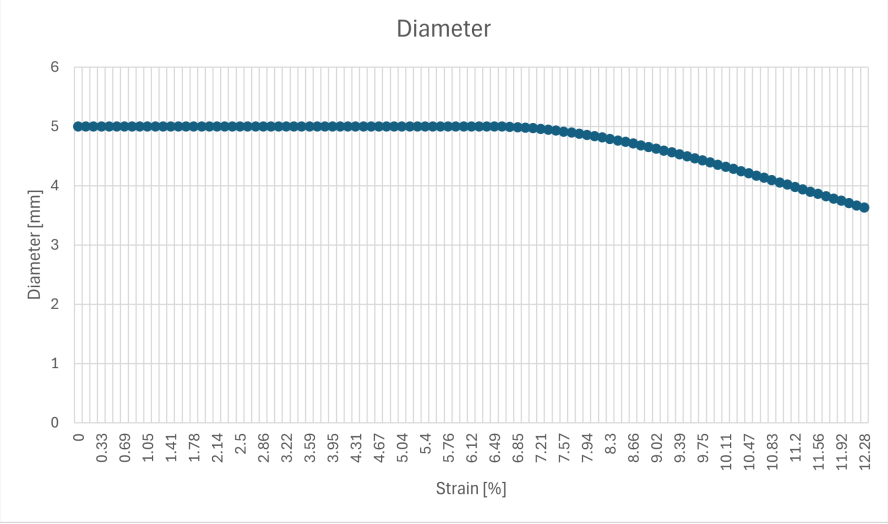

Figure 4.34: Diameter's change as a function of strain

4.8 Test six

It was also necessary to verify the reproducibility of the test performed at RT. the test was carried out in air as the controlled atmosphere was not required, givem the oxidation is not an issue at 25°C.

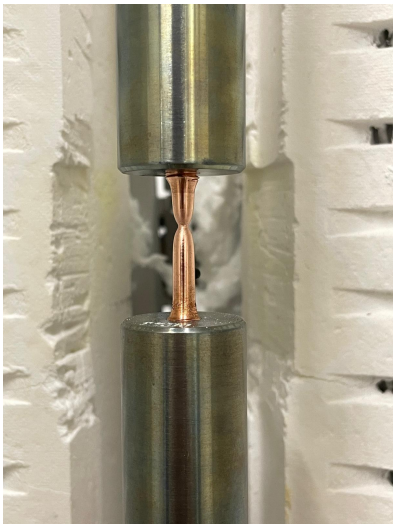

Figure 4.35: Specimen after test at RT

The same procedures and instruments used in the previous tests were implemented for the capture of the frames (Fig. 4.36).

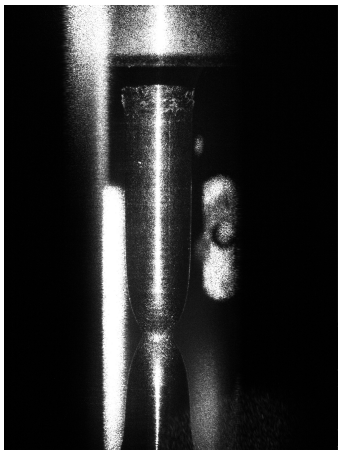

Figure 4.36: Frame obtained from test at RT

The same Python script was used to track the evolution of the diameter decrease in the necking area. Subsequently, the plot of the change of diameter as a function of the time (Fig. 4.37) was generated.

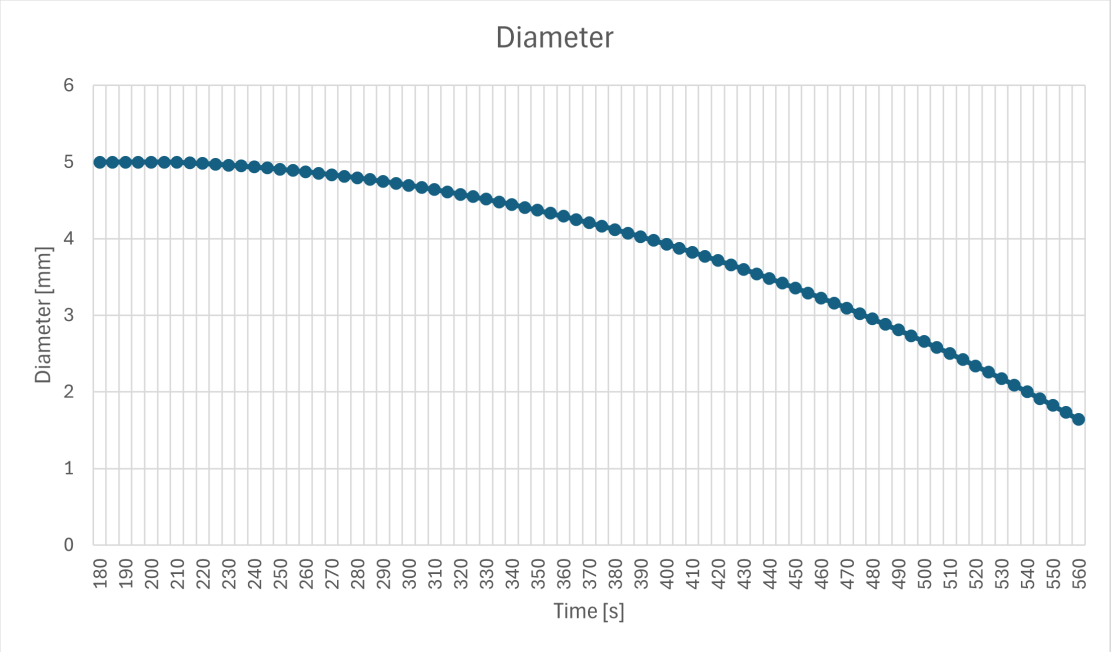

Figure 4.37: Diameter's change as a function of time

Then, using the force applied on the specimen during the test and the equation 4.1, it is possible to obtain the true stress as a function of time. The plot of the diamenter's decrement as a function of the true stess is generated (Fig. 4.38).

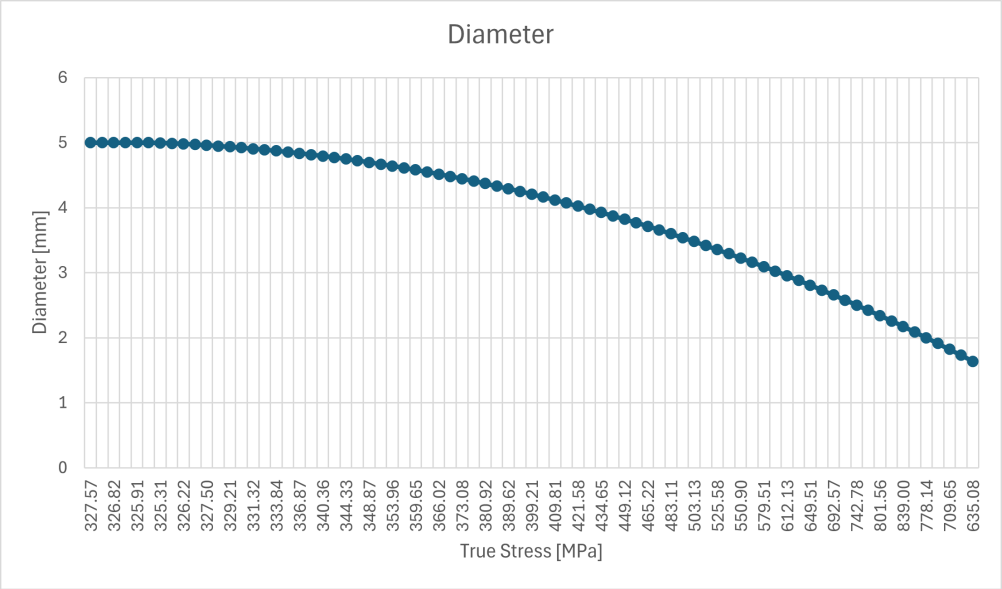

Figure 4.38: Diameter's change as a function of true stress

The complete evolution of the diameter as a fuction of the strain in shown in the following plot.

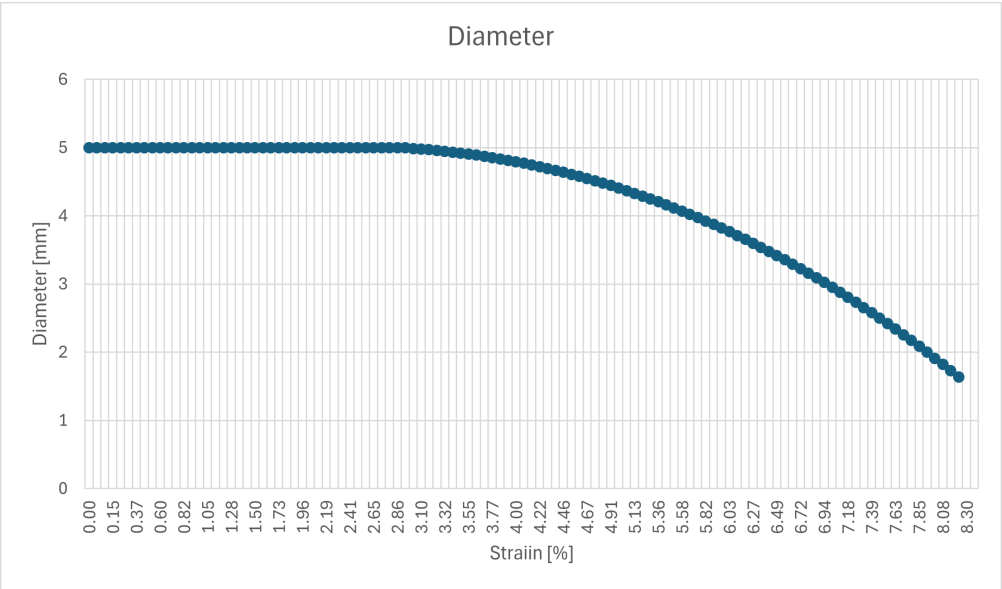

Figure 4.39: Diameter's change as a function of strain

It is important to note a problem that occured during the testing at RT. The specimen underwent a tensile load that reached a value of 6000 N before the measurement was abruptly interrupted due to a problem with the LaserXTens. Unfortunately, it was not possible to analyze the effect of these initial applied forces on the specimen for this portion of the test. The impact of this issue can be observed by comparing the two tests conducted at RT (par. 4.9).

4.9 Comparison between test four and test six

To do a comprehensive analysis of the necking phenomenon, it is essential to compare the results obtained from the two tests performed at RT.
Examining the stress-strain curves of the two measurements reveals no significant differences between their values.

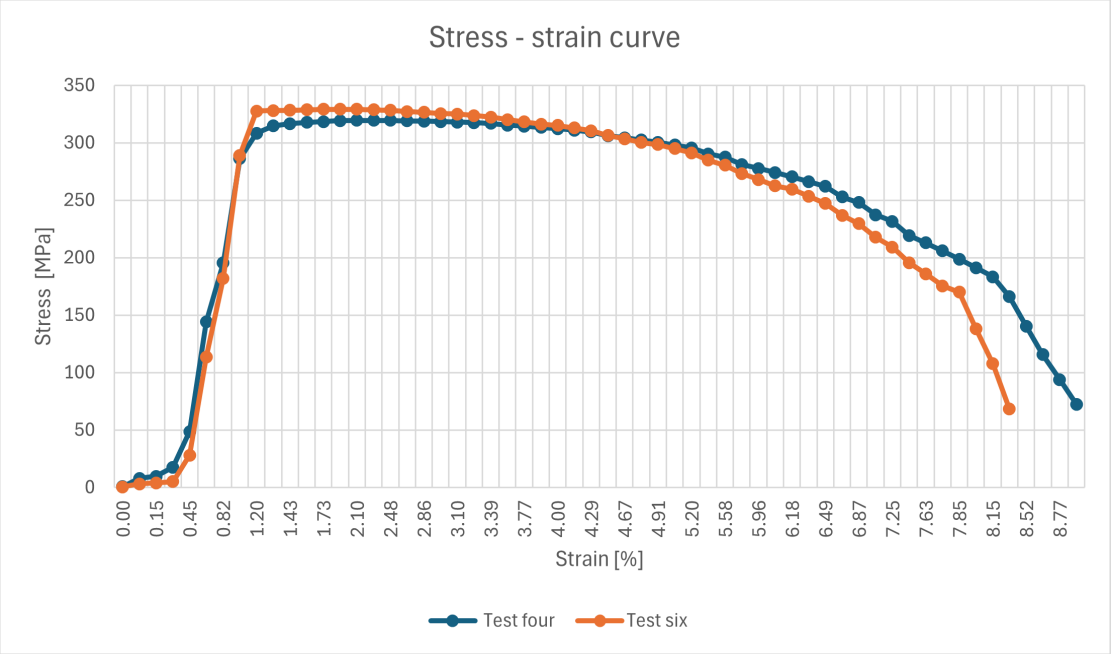

Figure 4.40: Comparison of stress-strain curve at RT

An important aspect to evaluate is that during test six (blue line in Fig. 4.40), the specimen reaches failure at a lower strain compared to the specimen after test four. Specifically, sample six fails at a strain value of 8.37%, while sample four at 8.90%. There is a difference of 0.53%, which is not significant. From this data, it appears that the issue described in paragraph 4.8, regarding the initial loading on the specimen that was not captured by the machine, did not significantly affect the results of the test.

However, when examining the graph of the diameter as a function of strain, a more pronounced difference is observable.

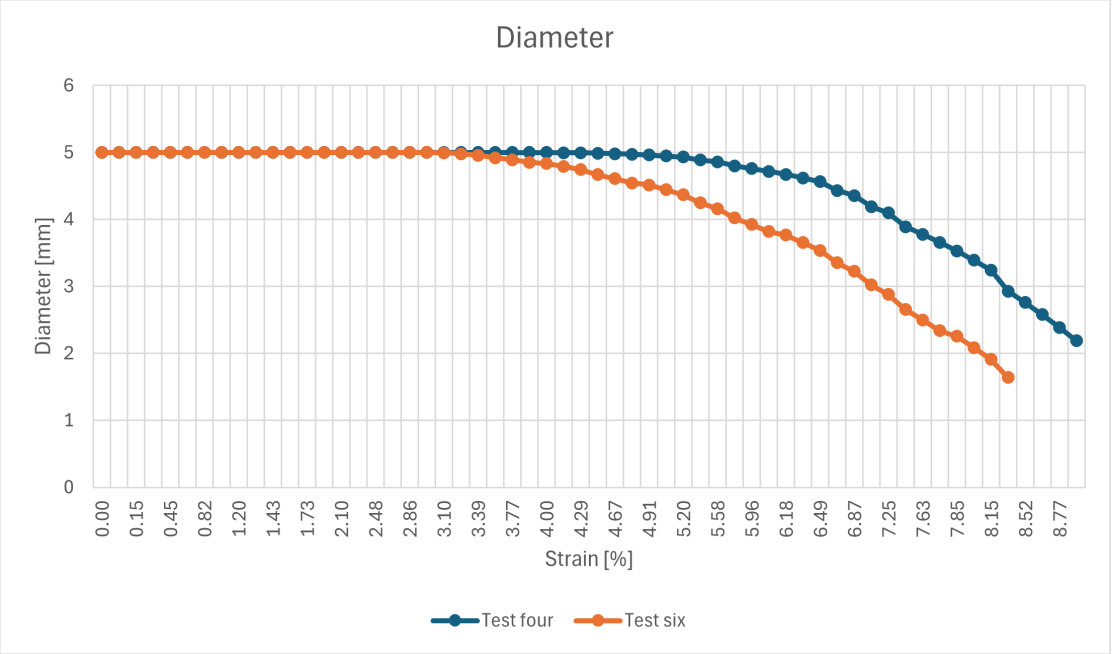

Figure 4.41: Comparison of diameter's change as a function of strain at RT

In test six there is a more significant decrease in the diameter despite similar strain values. At failure, the diameter measures 1.64 mm, in comparison to 2.19 mm for the specimen after test four. The difference is further illustrated in Figure 4.42, where the specimen from test four is shown at the top, and the specimen from test six is displayed at the bottom. Altough the length of the specimen after test four and six are similar (31 mm and 29 mm, respectively), the diameters exhibit a notable difference.

Figure 4.42: Difference in geometry after test at RT

The reason for this differentiation lies in the initial loading prior to test six. The specimen was subjected to a force of 6000 N before the measurement was halted. Given the initial area with a diameter of 5 mm, the applied stress would be approximately 306 MPa. Referring to the stress-strain curve (Fig. 4.40), this stress value is close to the maximum stress applied before the onset of the hardening phenomenon. As a result, the sample may have experienced an initial reduction in diameter along its entire length. However, this change could not be verified, as the results were not captured by the machine.

4.10 Comparison between test three and test five

By comparing the change in diameter as a function of strain from the two tests at 600°C, it is possible to verify the reproducibility of the meeasurements.

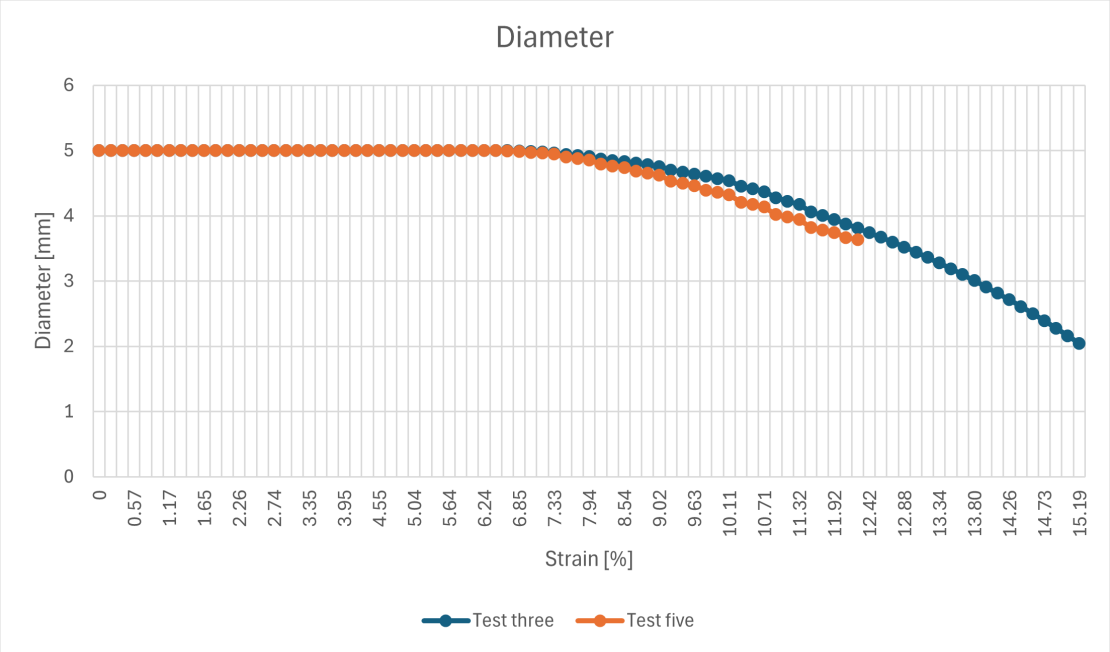

Figure 4.43: Comparison of diameter's change as a function of strain at 600°C

The values of the diameter during the necking phenomenon are similar, with a maximum standard deviation of 0.18, which indicates a coefficient of variation of 4.4%, an acceptable level of variability.

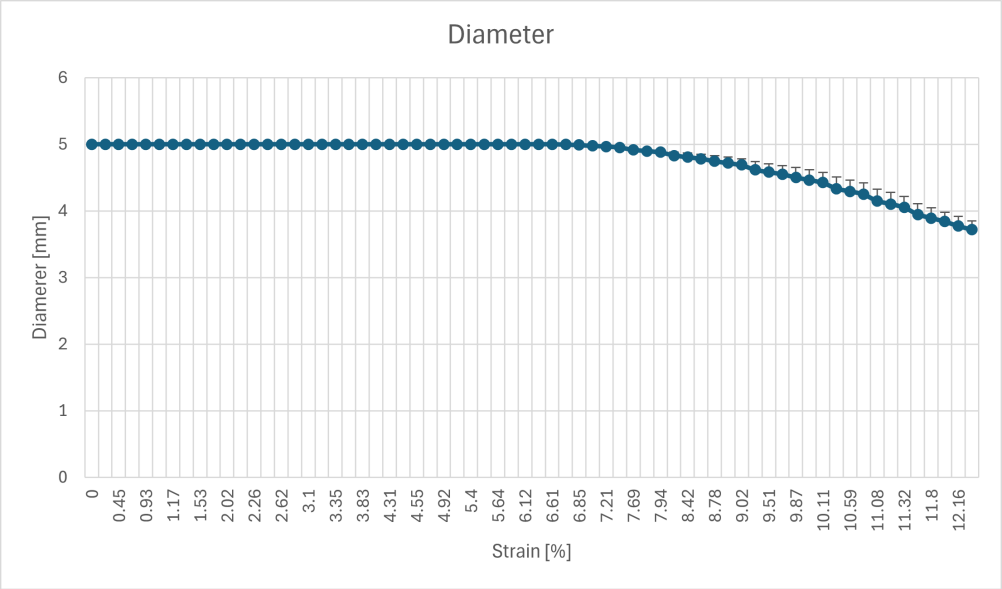

Figure 4.44: Standard deviation of diameter's change at high temperature

However, the sample reaches failure at a lower strain during test five in comparison to test three, with values of 12.28% and 15.19%, respectively. Additionally, the diameter at failure varies significantly between test three and test five: measuring 2.98 mm and 3.63 mm, respectively. The difference can be observed in the image of the two specimens after the tests (Fig. 4.45, with the top sample from test three, and the bottom sample from test five).

Figure 4.45: Difference in geometry after test at 600°C

The one from October is shorter and wider.

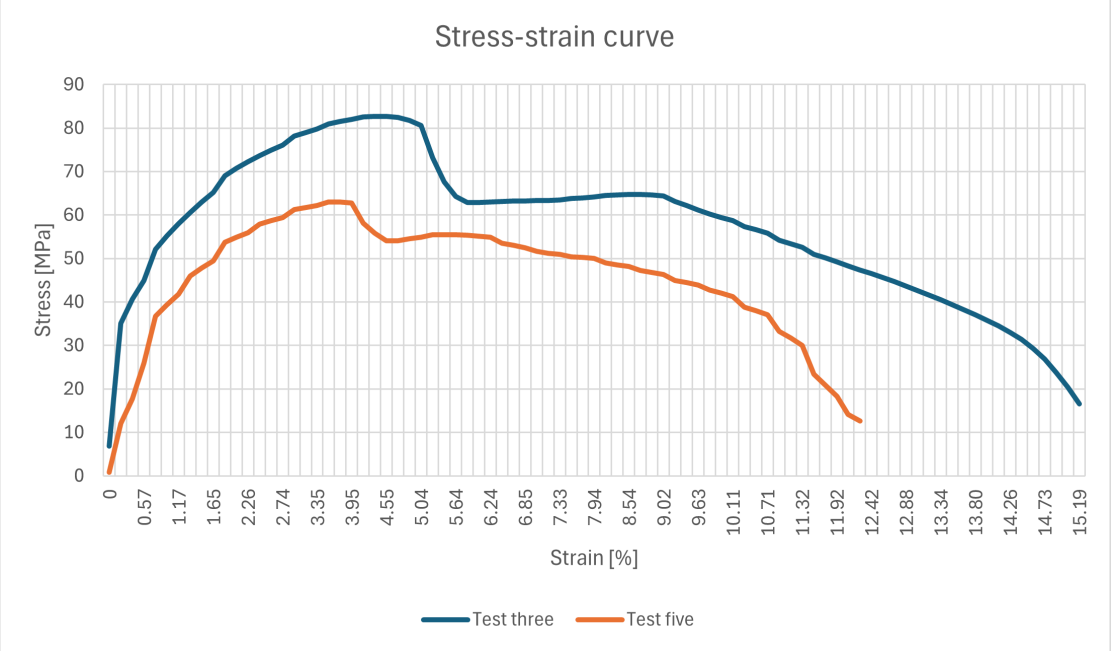

Figure 4.46: Comparison of stress-strain curve at 600°C

Analyzing the stress-strain curves (Fig. 4.46), it is evident that the stress applied to the specimen of the same geometry varies greatly: the maximum stress for the test three is approximately 82.68 MPa at a strain of 4.59%, whereas the maximum stress obtaind in test five is 63.04 MPa at a strain of 3.71%.
This difference can be attributed to the argon flow during the test. During test five, the argon flow was stronger, resulting in greater cooling of the specimen compared to the previous test at 600°C. This cooling effect decreases the ductility of the material, causing the sample to reach failure at a lower strain with a correspondingly lower applied stress. However, when compared to the tests performed at RT, the stresses applied are still lower.

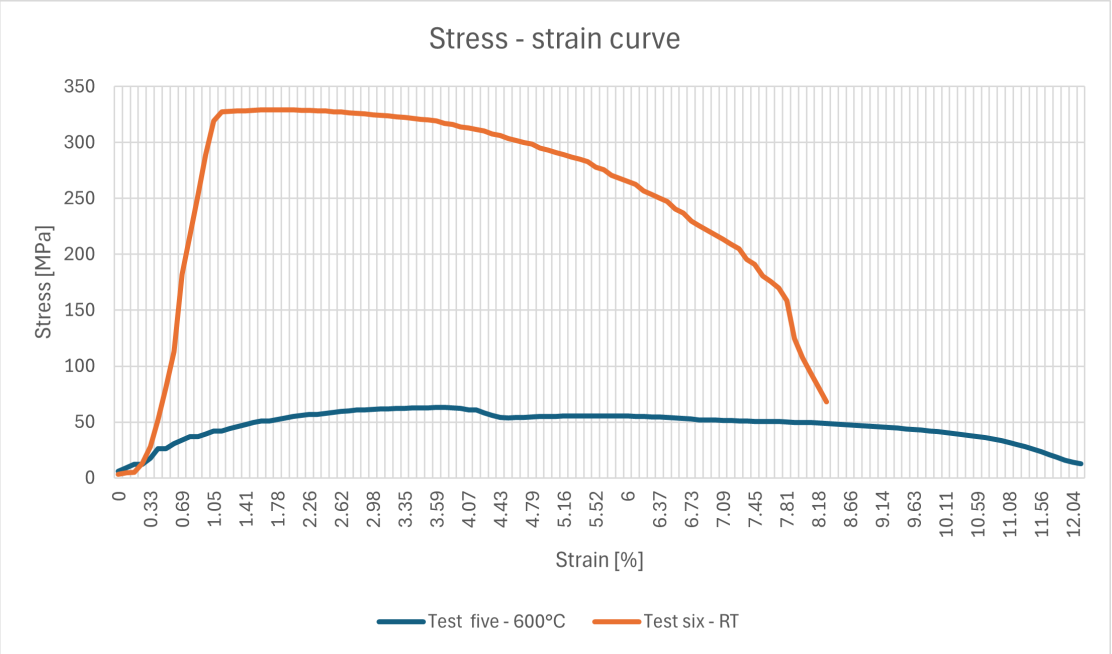

Figure 4.47: Comparison of stress-strain curve at RT and 600°C

Even if the specimen itself did not reach 600°C, as indicated by the oven temperature, it was still at a sufficiently high temperature to enhanced its ductility compared to the material tested at RT.

Figure 4.48: Difference in geometry after test at 600°C and RT

Chapter 5

Radius of curvature

5.1 Introduction

As mentioned in the introduction of the *Necking* chapter (ch. 4, par. 4.1), once necking begins, the distribution of strain and stress on the specimen becomes more complex, resulting in a triaxial stress state with a non-uniform pressure distribution across the necking region [44]. Due to this complexity, determining the true stress-true strain curve of a material post-necking requires calculating both the diameter in the necking area and the radius of its curvature [45].
The following paragraphs describe a method that uses frames obtained from tensile tests to track the evolution of changes in the radius of curvature.

5.2 Method

To obtain the evolution of the radius of curvature as a function of true stress, similar to the analysis performed for diameter change in the *Necking* chapter (ch. 4), a Python script was developed. Using frames from the previous tests conducted to measure diameter changes, the same sharpening filter previously applied was also applied to these images. The resulting images were cropped in the necking area.

However, in this case, instead of a single point, five points needed to be identified to apply the Ordinary Least Square (OLS) method. This method allows for the determination of the circumference that best describes the radius of curvature, as this technique finds the curve that fits closest to a given data set. The circumference is defined as

$$(x - a)^2 + (y - b)^2 = r^2$$

where *(a,b)* are the coordinates of the center, and r is the radius of the circle. The OLS method calculates the distance from each data point to the candidate center. Then, the difference between the measured distance and the estimated radius is squared to give the error for each point. These squared errors are summed, and the values of the center and radius that minimize the total squared error are determined. This approach identifies the circle that best fits the points.
This method was implemented in Python through a *FindCircle* function, which uses matrix operations to determine the radius and center values based on the five points identified on the specimen.
The results of this implemetation are shown in the next paragraph (par. 5.3).

5.3 Results

Initially, the frames from test three (ch. 4, par. 4.4) were selected for the analysis to establish a reliable method, as these frames were cleaner and offered higher contrast, making them more suitable for accurate measurement (Fig. 4.12). Following the method outlined in the paragraph *Method* (par. 5.2), the corresponding points and circumferences describing the radius of curvature were identified at three different moments during the tensile test.

Frame 700, 900, and 1120 were analyzed: the first corresponds to the onset of more pronounced necking, frame 900 represents a midpoint from when the necking is detected by the program, and 1120 marks the end of the test.

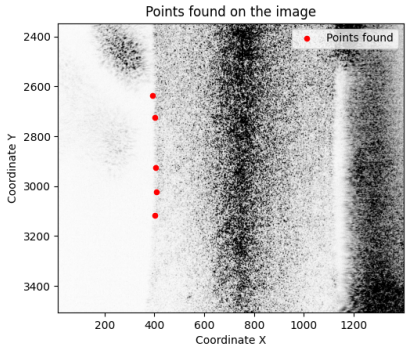

Figure 5.1: Points found in frame 700

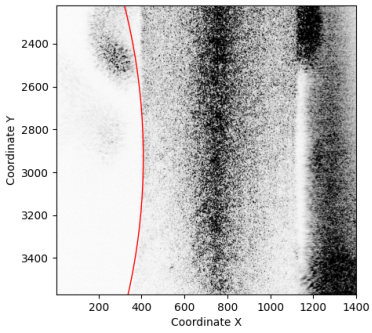

Figure 5.2: Circumference in frame 700

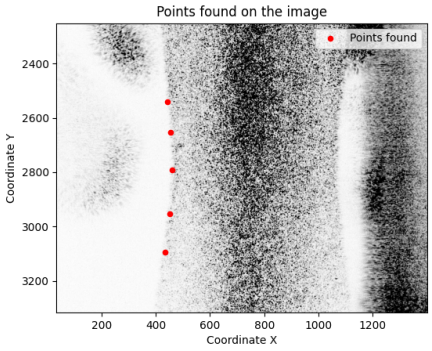

Figure 5.3: Points found in frame 900

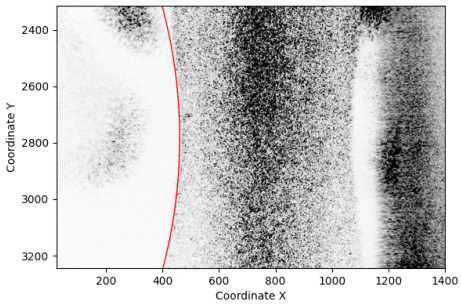

Figure 5.4: Circumference in frame 900

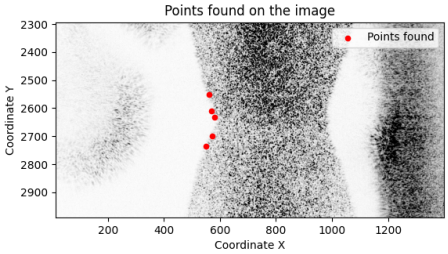

Figure 5.5: Points found in frame 1120

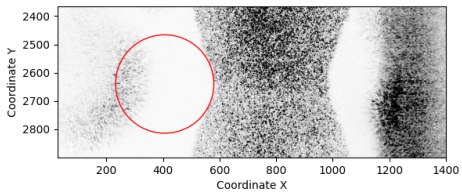

Figure 5.6: Circumference in frame 1120

A third-degree polynomial was fitted to the raw data obtained from the Python script to achieve a smoother and more continuous representation of the radius of curvature change evolution.

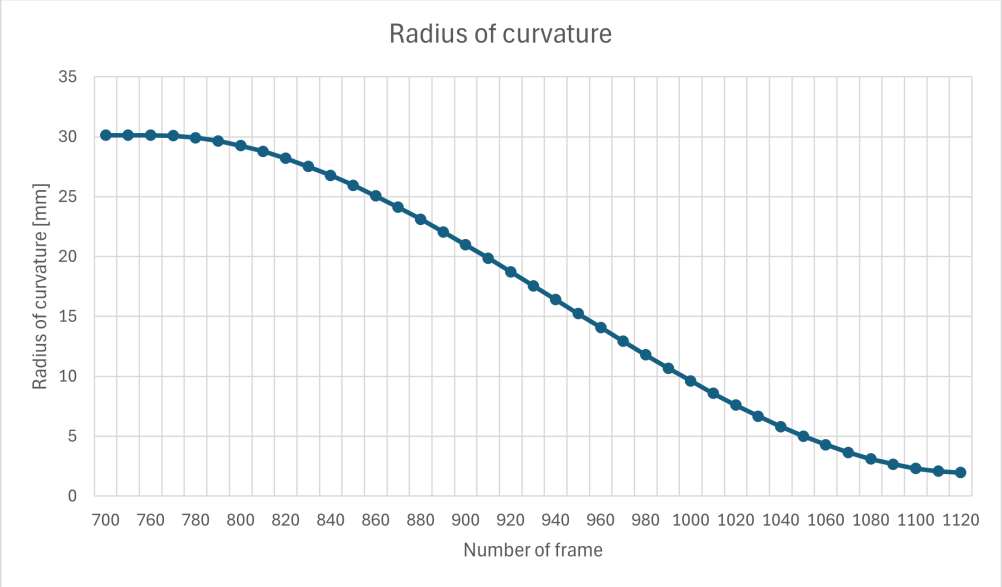

Figure 5.7: Evolution of the radius of curvature as a function of frame number

The same method used to correlate the frame number to the true stress during the diameter change analysis was also applied to the radius of curvature. Utilizing the time parameter, it becomes possible to track the complete evolution of the

radius of curvature as a function of true stress, as shown in Figure 5.8.

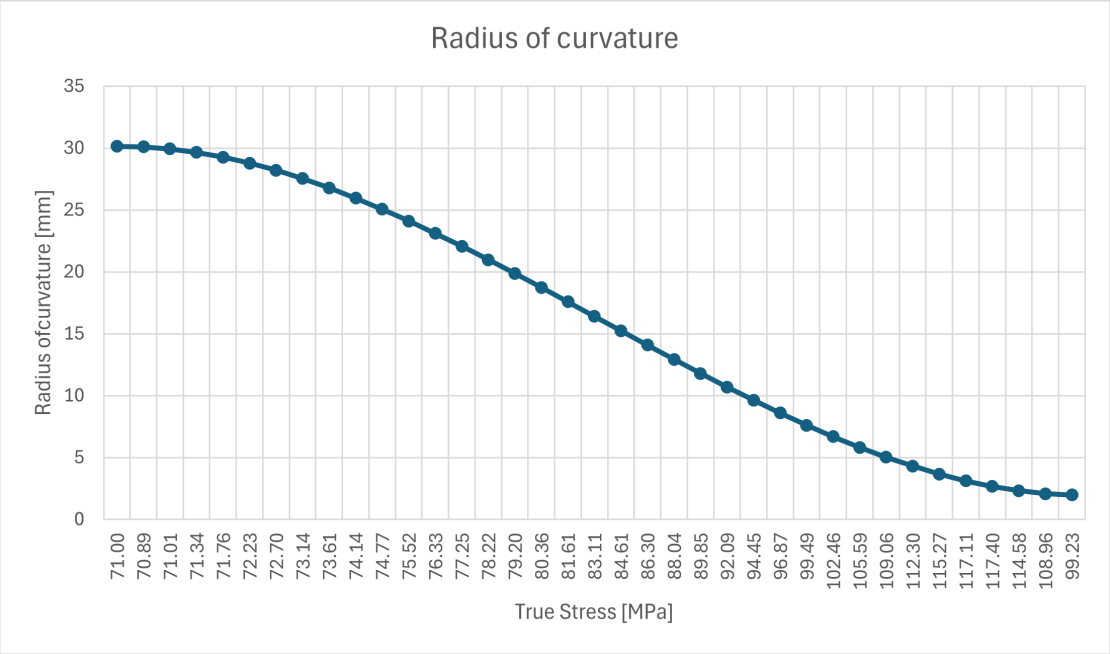

Figure 5.8: Evolution of the radius of curvature as a function of true stress

The change in the radius of curvature begins with the onset of necking. Prior to this, in the absence of curvature, the radius of curvature is considered infinite. It is important to analyze how the radius of curvature progresses in relation to the change in diameter.

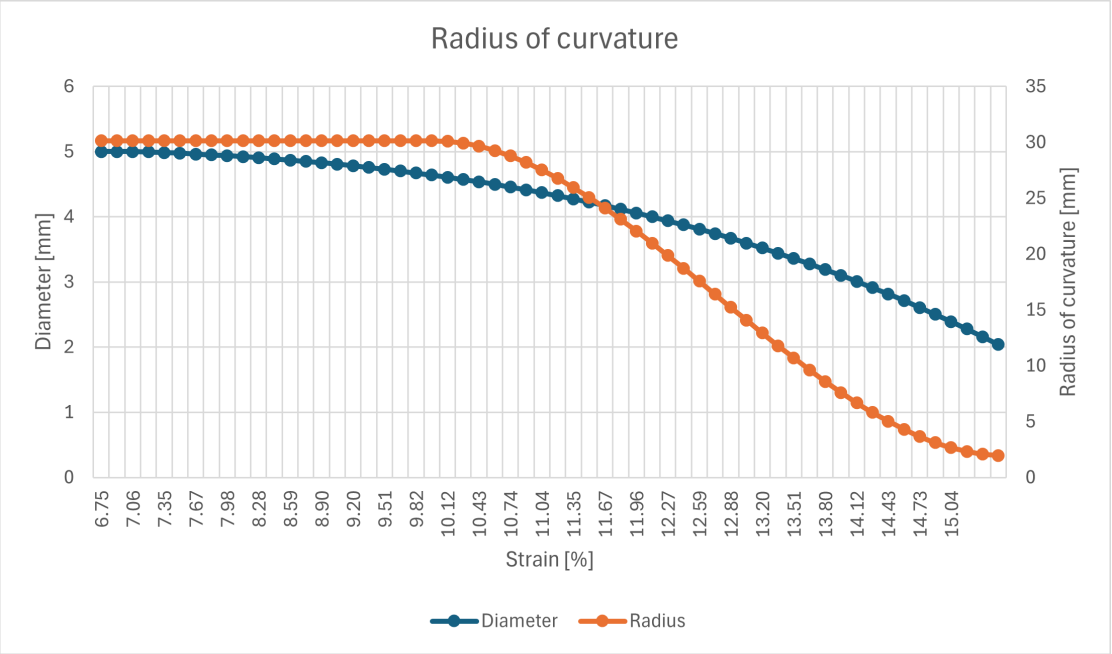

Figure 5.9: Evolution of radius of curvature and diameter as function of the strain

As shown in figure 5.9, although necking initiates at a strain of 6.89%, the Python program developed to evaluate the radius of curvature detects a significant change only at a strain of 9.66%. This discrepancy arises from the nature of the Python program. Unlike a machine that measures variations continuously during the tensile test, the program relies on post-processing images. Although the image quality is high, there is still noise that affects the program's accuracy. Consequently, smaller changes are often missed, and only larger variations are captured, allowing the program to evaluate the evolution.

Conclusion

This thesis focused on characterizing innovative materials for fusion applications within the European EUROfusion program, which aims to establish the foundation for the commercialization of energy from fusion power reactors. Specifically, this work centers on the characterization of the copper alloy CuCrZr, which is a prime candidate as a structural material for the heat sink in the divertor for ITER and DEMO. The study of the thesis is divided into mechanical and thermo-mechanical characterization. It also includes the analysis of the evolution of the diameter and radius of curvature.

The mechanical characterization involved evaluating the elastic modulus, E, across the operational temperature range, from room temperature up to 600°C, in controlled atmosphere, in order to minimize the influence of the oxidized layer.
Additionally, using a different set-up, the elastic modulus evaluation was extended to include measurements of the shear modulus, G, and Poisson ratio, μ. These measurements were conducted within the same temperature range as the initial evaluation of Young modulus, also in a controlled atmosphere. The results align with expectations based on existing literature.

The thermo-mechanical characterization focused primarily on determining the coefficient of linear thermal expansion (CTE) from room temperature up to 600°C

in controlled atmosphere. All tests were performed on the same CuCrZr specimen, which influenced the results: each subsequent evaluation of CTE showed an increase due to cumulative heat treatments. For future analyses, repeating the measurements on a separate specimen of the same geometry would help confirm test reproducibility, as using the same sample for all tests may have affected the results.

Furthermore, to fully evaluate the behavior of CuCrZr under tensile testing, in particular after the onset of necking, when stress-strain distribution becomes more complex, the evolution of the diameter and the radius of curvature were analyzed. It was essential to first establish a reliable method for this analysis; therefore, initial tests for calculating these variables were conducted on a 5 mm diameter cylindrical specimen of pure copper, instead of CuCrZr. The approach chosen for this analysis involved the post-processing of frames captured during the tensile test using a Python script. Initially, only the evolution of the diameter was considered.
Six tensile tests were conducted to obtain the necessary images for the evaluation. The first two tests were performed at RT, using a USB camera to capture the frames. However, these initial tests did not allow for the required evaluation of the diameter evolution as a function of true stress, as no common parameter could be established between the applied force and the diameter evolution.
The following tests were then performed using LaserXTens to caputre the images for the evaluation. These remaining four tests, two at 600°C and two at RT, were able to provide satisfying results: the evolution of the diameter as a function of true stress was successfully obtained. This enabled the construction of the true stress-strain curve for both the 600°C and RT tests.

The first test at 600°C (referred to as test three in this thesis) conducted with LaserXTens was utilized to establish a reliable method for tracking the evolution of the radius of curvature. The analysis was carried out by developing a Python

script that employed the OLS method to calculate the circumference intersecting the necking region.

The next steps to complete the characterization involve applying the Python scripts developed for tracking the evolution of the diameter and the radius of curvature in pure copper to the frames that will be obtained from tests conducted on CuCrZr.

Bibliography

[1] Iea - International Energy Agency. *World Energy Outlook 2023*. 2023. URL: www.iea.org/terms (cit. on p. 1).

[2] European Commission and Directorate-General for Communication. *European green deal – Delivering on our targets*. Publications Office of the European Union, 2021 (cit. on p. 1).

[3] Qiang Wang, Jiale Guo, Rongrong Li, and Xue ting Jiang. «Exploring the role of nuclear energy in the energy transition: A comparative perspective of the effects of coal, oil, natural gas, renewable energy, and nuclear power on economic growth and carbon emissions». In: *Environmental Research* 221 (Mar. 2023) (cit. on p. 1).

[4] Danish, Recep Ulucak, and Seyfettin Erdogan. «The effect of nuclear energy on the environment in the context of globalization: Consumption vs production-based CO2 emissions». In: *Nuclear Engineering and Technology* 54 (4 Apr. 2022), pp. 1312–1320 (cit. on p. 1).

[5] D. Lerede, M. Nicoli, L. Savoldi, and A. Trotta. «Analysis of the possible contribution of different nuclear fusion technologies to the global energy transition». In: *Energy Strategy Reviews* 49 (Sept. 2023) (cit. on p. 1).

[6] -Prof TU Dieter Breitschwerdt Berlin, -Prof Richard Pitts, Paul Lez Durance -Dr Roberto Bilato, -Dr Ralph Dux Boltzmannstr, -Dr Thomas Hamacher, Hans-Stephan Bosch, -Dr Matthias Hirsch Wendelsteinstr, -Dr Ralf Kleiber D-, and Greifswald -Dr Heinrich Laqua. *List of speakers* (cit. on pp. 1, 2).

[7] A. M. Bradshaw, T. Hamacher, and U. Fischer. «Is nuclear fusion a sustainable energy form?» In: *Fusion Engineering and Design* 86 (9-11 Oct. 2011), pp. 2770–2773 (cit. on p. 2).

[8] https://www.iter.org/newsline/-/3071. *Will fusion run out of fuel?* July 2018 (cit. on p. 2).

[9] T Tone et al. *Fusion Reactor Design and Technology Vol.I, Proceedings of the third technical Committee Meeting and WQorkshop, Tokyo, 5-16 October 1981* (cit. on p. 2).

[10] L Spitzer. *The Stellarator Concept* (cit. on p. 2).

[11] M Victoria, N Baluc, and P Spätig. *Structural Materials for Fusion Reactors* (cit. on p. 2).

[12] T Muroga, M Gasparotto, and S J Zinkle. *Overview of materials research for fusion reactors* (cit. on p. 2).

[13] P.-H. Rebut. «ITER: the first experimental fusion reactor». In: *Fusion Engineering and Design* 30.1 (1995), pp. 85–118 (cit. on p. 4).

[14] Long Version. *European Research Roadmap to the Realisation of Fusion Energy* (cit. on pp. 4–7).

[15] *The ITER fusion experiment J Dietz and the ITER Joint Central Team, lTER Garching Joint Work Site.* 1996 (cit. on pp. 4, 5).

[16] V. Barabash et al. «Materials challenges for ITER - Current status and future activities». In: *Journal of Nuclear Materials* 367-370 A (SPEC. ISS. Aug. 2007), pp. 21–32 (cit. on p. 5).

[17] Mario Merola, Frederic Escourbiac, René Raffray, Philippe Chappuis, Takeshi Hirai, and Alex Martin. «Overview and status of ITER internal components». In: *Fusion Engineering and Design*. Vol. 89. Elsevier Ltd, 2014, pp. 890–895 (cit. on p. 5).

[18] T. Hirai, V. Barabash, F. Escourbiac, A. Durocher, L. Ferrand, V. Komarov, and M. Merola. «ITER divertor materials and manufacturing challenges». In: *Fusion Engineering and Design* 125 (Dec. 2017), pp. 250–255 (cit. on p. 5).

[19] L. M. Giancarli et al. «Overview of the ITER TBM Program». In: *Fusion Engineering and Design*. Vol. 87. Aug. 2012, pp. 395–402 (cit. on p. 5).

[20] G. Federici, L. Boccaccini, F. Cismondi, M. Gasparotto, Y. Poitevin, and I. Ricapito. «An overview of the EU breeding blanket design strategy as an integral part of the DEMO design effort». In: *Fusion Engineering and Design* 141 (Apr. 2019), pp. 30–42 (cit. on p. 5).

[21] Mohamed Abdou, Neil B. Morley, Sergey Smolentsev, Alice Ying, Siegfried Malang, Arthur Rowcliffe, and Mike Ulrickson. *Blanket/first wall challenges and required RD on the pathway to DEMO*. Nov. 2015 (cit. on pp. 5, 6).

[22] *2017 IEEE International Conference on Environment and Electrical Engineering and 2017 IEEE Industrial and Commercial Power Systems Europe (EEEIC)*. IEEE, 2017 (cit. on p. 6).

[23] Suk Ho Hong. *A review of DEMO reactor concepts: open questions and issues*. Dec. 2022 (cit. on p. 6).

[24] G. Federici, J. Holden, C. Baylard, and A. Beaumont. «The EU DEMO staged design approach in the Pre-Concept Design Phase». In: *Fusion Engineering and Design* 173 (Dec. 2021) (cit. on p. 6).

[25] J W Coenen et al. «Materials for DEMO and reactor applications-boundary conditions and new concepts». In: *Physica Scripta* T167 (2015), p. 014002 (cit. on p. 6).

[26] M. Gorley, G. Aiello, J. Henry, T. Nozawa, G. Pintsuk, M. Rieth, and H. Tanigawa. «DEMO structural materials qualification and development». In: *Fusion Engineering and Design* 170 (2021), p. 112513 (cit. on p. 6).

[27] Thilo Grammes, Thomas Emmerich, Dandan Qu, Oliver Heinze, Robert Vaßen, and Jarir Aktaa. «Functionally graded tungsten/EUROFER coating for DEMO first wall: From laboratory to industrial production». In: *Fusion Engineering and Design* 188 (2023), p. 113430 (cit. on p. 6).

[28] EUROfusion. *EUROfusion - RealiSing Fusion Energy.* `https://euro-fusion.org/eurofusion/` (cit. on p. 7).

[29] Gerald Pintsuk, Eberhard Diegele, Sergei L. Dudarev, Michael Gorley, Jean Henry, Jens Reiser, and Michael Rieth. «European materials development: Results and perspective». In: *Fusion Engineering and Design* 146 (Sept. 2019), pp. 1300–1307 (cit. on p. 7).

[30] M. Li and S. J. Zinkle. «4.20 - Physical and Mechanical Properties of Copper and Copper Alloys». In: vol. 1-5. Elsevier, Jan. 2012, pp. 667–690 (cit. on p. 8).

[31] Kuo Zhang, Ermile Gaganidze, and Michael Gorley. «Development of the material property handbook and database of CuCrZr». In: *Fusion Engineering and Design* 144 (July 2019), pp. 148–153 (cit. on p. 8).

[32] S. D. Preston, I. Bretherton, and C. B.A. Forty. «The thermophysical and mechanical properties of the copper heat sink material intended for use in ITER». In: *Fusion Engineering and Design*. Vol. 66-68. Sept. 2003, pp. 441–446 (cit. on p. 8).

[33] *Elastic Modulus Measurement Elastic Modulus Measurement A NATIONAL MEASUREMENT GOOD PRACTICE GUIDE* (cit. on pp. 10, 12, 16).

[34] *Standard Test Method for Dynamic Young's Modulus, Shear Modulus, and Poisson's Ratio by Impulse Excitation of Vibration 1* (cit. on pp. 10, 11, 24).

[35] ITER organization. *ITER material properties handbook* (cit. on pp. 16, 17).

[36] Paweł Ostachowski, Włodzimierz Bochniak, Marek Łagoda, and Stanisław Ziółkiewicz. «Strength properties and structure of CuCrZr alloy subjected to low-temperature KOBO extrusion and heat treatment». In: *International Journal of Advanced Manufacturing Technology* 105 (12 Dec. 2019), pp. 5023–5044 (cit. on p. 22).

[37] Yehuda Partom. «Change of shear modulus and yield stress with pressure and temperature». In: *AIP Conference Proceedings* 1793.1 (Jan. 2017), p. 110018 (cit. on p. 29).

[38] Daeho Kim, Sungjun Lee, Sang Hyun Lee, and Suyong Kwon. «Measurement of Thermal Expansion over a Wide Range of Temperatures by a Pushrod Dilatometer». In: *Journal of the Korean Physical Society* 77 (6 Sept. 2020), pp. 496–504 (cit. on pp. 31–33).

[39] J D James, J A Spittle, S G R Brown, and R W Evans. *A review of measurement techniques for the thermal expansion coefficient of metals and alloys at elevated temperatures*. 2001 (cit. on pp. 31, 32).

[40] Ru-Min Wang, Shui-Rong Zheng, and Ya-Ping Zheng. «11 - Other properties of polymer composites». In: *Polymer Matrix Composites and Technology*. Ed. by Ru-Min Wang, Shui-Rong Zheng, and Ya-Ping Zheng. Woodhead Publishing Series in Composites Science and Engineering. Woodhead Publishing, 2011, pp. 513–548. URL: https://www.sciencedirect.com/science/article/pii/B9780857092212500114 (cit. on p. 31).

[41] Winston H Chent. *NECKING OF A BAR*. 1971 (cit. on p. 38).

[42] K. Huang and R.E. Logé. «A review of dynamic recrystallization phenomena in metallic materials». In: *Materials Design* 111 (2016), pp. 548–574 (cit. on p. 55).

[43] The Editors of Encyclopaedia Britannica. «ductility». In: *Encyclopedia Britannica* (2 Sep. 2024) (cit. on p. 62).

[44] Feng Lu, Tomáš Mánik, Ida Lægreid Andersen, and Bjørn Holmedal. «A Robust Image Processing Algorithm for Optical-Based Stress–Strain Curve Corrections after Necking». In: *Journal of Materials Engineering and Performance* 30 (6 June 2021), pp. 4240–4253. ISSN: 15441024. DOI: 10.1007/s11665-021-05777-2 (cit. on p. 77).

[45] Mikhail V Erpalov, Danis Sh Nukhov, and Dmitry A Pavlov. «MATHEMATICAL MODEL OF NECK FORMATION DURING TENSILE TESTING OF CYLINDRICAL SPECIMEN». In: *Journal of Chemical Technology and Metallurgy* (2020) (cit. on p. 77).